

Metallicity Gradients in the Intracluster Gas of Abell 496

Renato A. Dupke & Raymond E. White III

Department of Physics and Astronomy, University of Alabama,
Box 870324, Tuscaloosa, AL 35487-0324

ABSTRACT

Analysis of spatially resolved *ASCA* spectra of the intracluster gas in Abell 496 confirms there are mild metal abundance enhancements near the center, as previously found by White et al. (1994) in a joint analysis of *Ginga* LAC and *Einstein* SSS spectra. Simultaneous analysis of spectra from all *ASCA* instruments (SIS + GIS) shows that the iron abundance is 0.36 ± 0.03 solar $3 - 12'$ from the center of the cluster and rises $\sim 50\%$ to 0.53 ± 0.04 solar within the central $2'$. Nickel and sulfur abundances are also centrally enhanced. We use a variety of elemental abundance ratios to assess the relative contribution of SN Ia and SN II to the metal enrichment of the intracluster gas. We find marginal evidence of gradients in some abundance ratios, which indicate that the fraction of iron from SN Ia increases toward the cluster center. We estimate that SN Ia account for $\sim 46\%$ of the iron mass $3 - 12'$ from the center and $\sim 72\%$ within $2'$. The increased proportion of SN Ia ejecta at the center is such that the central iron abundance enhancement can be attributed wholly to SN Ia; we find no significant gradient in SN II ejecta. We argue that the additional SN Ia ejecta near the center is the vestige of a secondary wind phase driven by SN Ia (following a more vigorous protogalactic wind driven by SN II), which was partially smothered in the cD due to its location at the cluster center. We argue against the central abundance enhancement being due to ram pressure stripping of gas from cluster galaxies, or to secularly accumulated stellar mass loss within the central cD, or to a radially declining ratio of early-type galaxy luminosity density to intracluster gas density.

Subject headings: galaxies: abundances — galaxies: clusters: individual (Abell 496) — intergalactic medium — X-rays: galaxies

1. Introduction

While the metals observed in intracluster gas clearly originate from stars, it remains controversial how the metals got from stars into the intracluster gas. The two metal enrichment mechanisms considered to be most likely are protogalactic winds from early-type galaxies (Larson & Dinerstein 1975) and ram pressure stripping of gas from galaxies (Gunn & Gott 1972). Early *Einstein* FPCS spectroscopy (Canizares et al. 1982) and more recent *ASCA* spectroscopy (Mushotzky & Loewenstein 1997; Mushotzky et al. 1996) showed that global intracluster metal abundances are consistent with ejecta from Type II supernovae, which supports the protogalactic wind model. White (1991) showed that the specific energy of intracluster gas is greater than that of cluster galaxies, which also suggests that protogalactic winds injected significant amounts of energy and metals into intracluster gas. However, theoretical uncertainties about the elemental yields from Type II supernovae make it difficult to determine confidently the relative proportion of iron from SN II and SN Ia in intracluster gas (Gibson, Loewenstein & Mushotzky 1997). This uncertainty has allowed others to conclude that as much as $\sim 50\%$ of the iron in intracluster gas comes from SN Ia (Ishimaru & Arimoto 1997; Nagataki & Sato 1998). The possible presence of such large quantities of iron from SN Ia is problematic. Is it ejecta from a secondary SN Ia-driven wind phase in ellipticals? Or is ram pressure so effective that it contaminates the outer parts of clusters nearly as effectively as the central regions?

An increasing number of galaxy clusters are being found with centrally enhanced metal abundances in their intracluster gas. *Ginga* observations of the Virgo cluster showed that its iron abundance declines from ~ 0.5 solar at the center to ~ 0.1 – 0.2 solar 3° away (Koyama, Takano & Tawara 1991). White et al. (1994) found central abundance enhancements in Abell 496 and Abell 2142 in joint analyses of *Ginga* LAC and *Einstein* SSS spectra. *ASCA* observations of the Centaurus cluster show that its iron abundance declines from \sim solar at the center to ~ 0.3 solar $15'$ away (Fukazawa et al. 1994). The Perseus cluster may also have an abundance gradient near its center (Ulmer et al. 1987; Ponman et al. 1990; Kowalski et al. 1993; Arnaud, et al. 1994). More recently, central abundance enhancements were found in *ASCA* data for Hydra A (Ikebe et al. 1997) and AWM 7 (Ezawa et al. 1997; Xu et al. 1997), as well as in *ROSAT* data for Abell 85 (Pislar et al. 1997). The presence of these central abundance enhancements is poorly correlated with global cluster properties. Although they seem to be more common in cool clusters, they can also occur in hot clusters. Thus far, all clusters observed with central metal enhancements also have central cooling flows; however, *most* clusters have cooling flows (Edge, Stewart & Fabian 1992), so it is not clear whether this fact is significant. Cluster mergers and the advective action of cooling flows may be obscuring possible correlations by washing out pre-existing abundance gradients.

There are several mechanisms which may cause central abundance enhancements in intracluster gas, including: 1) the spatial density of metal-injecting galaxies tends to decline more rapidly with radius than does the intracluster gas density, so the gas may be more contaminated at the center (Koyama et al. 1991; White et al. 1994); 2) ram pressure stripping of the metal-rich gas in cluster galaxies by intracluster gas is more effective at the center, where the intracluster gas density is highest (Nepveu 1981); 3) secular mass loss from the stars in central dominant galaxies may accumulate near the cluster center (White et al. 1994); 4) if early-type galaxies blew proto-galactic winds, such winds may be at least partially suppressed in central dominant galaxies, by virtue of their location at the bottom of their clusters’ gravitational potentials and in the midst of the highest intracluster gas density (White et al. 1994).

In this paper we analyze spatially resolved *ASCA* spectra of Abell 496 and confirm that it has centrally enhanced metal abundances. We argue that these central abundance enhancements are most likely due to the partial suppression of a secondary SN Ia-driven wind from the cD (following a more vigorous protogalactic wind driven by SN II), rather than any of the other three possible mechanisms cited above.

Abell 496 is a Bautz-Morgan Type I cluster with an optical redshift of $z = 0.0328$. Adopting a Hubble constant of $50 \text{ km s}^{-1} \text{ Mpc}^{-1}$ and $q_0 = 0.5$, its luminosity distance is $197 h_{50}^{-1} \text{ Mpc}$ and $1' = 57 h_{50}^{-1} \text{ kpc}$. The central cD (MCG -02-12-039) has a total B magnitude of $B_T = 13.42$ (Valentijn 1983) and an optical effective radius of $r_{\text{eff}} > 49 h_{50}^{-1} \text{ kpc}$ (Schombert 1986). Neither the projected galaxy distribution nor the galaxy velocity distribution in the cluster shows signs of significant substructure, so the cluster appears to be dynamically relaxed (Bird 1993; Zabludoff, Huchra & Geller 1990). Heckman (1981) was the first to suggest that Abell 496 contained a cooling flow, after he detected cool $\text{H}\alpha$ -emitting gas in its central cD galaxy; subsequent optical observations found extended $\text{H}\alpha$ emission (Cowie et al. 1983). Nulsen et al. (1982) found a soft X-ray component in *Einstein* SSS spectra of this cluster and estimated a cooling accretion rate of $\sim 200 M_{\odot} \text{ yr}^{-1}$, which is consistent with later analyses (Mushotzky 1984; Mushotzky & Szymkowiak 1988; Canizares, Markert & Donahue 1988; Thomas, Fabian & Nulsen 1987; White et al. 1994). In the course of a joint analysis of *Einstein* SSS and *Ginga* LAC spectra, White et al. (1994) found a central abundance enhancement in Abell 496; the differing fields of view of these two instruments allowed a coarsely spatially-resolved analysis. The *ASCA* observations of Abell 496 have been previously analyzed by Mushotzky (1995) and Mushotzky et al. (1996), who found no evidence of an abundance gradient within the central 1 Mpc; however, the first paper analyzed data from only one of the four *ASCA* spectrometers, while the second considered data from all four *ASCA* spectrometers, but only beyond $3'$ from the center (in order to avoid the spectral influence of the central cooling

flow). We include the central cooling flow region in our analysis of data from all four *ASCA* spectrometers.

2. Data Reduction & Analysis

ASCA carries four large-area X-ray telescopes, each with its own detector: two Gas Imaging Spectrometers (GIS) and two Solid-State Imaging Spectrometers (SIS). Each GIS has a 50' diameter circular field of view and a usable energy range of 0.7–12 keV; each SIS has a 22' square field of view and a usable energy range of 0.4–10 keV.

Abell 496 was observed for 40 ksec by *ASCA* on 20-21 September 1993. We selected data taken with high and medium bit rates, with cosmic ray rigidity values ≥ 6 GeV/c, with elevation angles from the bright Earth of $\geq 20^\circ$ and from the Earth's limb of $\geq 5^\circ$ (GIS) or 10° (SIS); we also excluded times when the satellite was affected by the South Atlantic Anomaly. Rise time rejection of particle events was performed on GIS data, and hot and flickering pixels were removed from SIS data. The resulting effective exposure times for each instrument are shown in Table 1. Since the cluster fills the spectrometers' fields of view, we estimated the background from blank sky files provided by the *ASCA* Guest Observer Facility.

We used XSPEC v9.0 (Arnaud 1996) software to analyze the SIS and GIS spectra separately and jointly. We fit spectra using the `mekal` and `vmekal` thermal emission models, which are based on the emissivity calculations of Mewe & Kaastra (cf. Mewe, Gronenschild & van den Oord 1985; Mewe, Lemen & van den Oord 1986; Kaastra 1992), with Fe L calculations by Liedahl, Osterheld & Goldstein (1995). Abundances are measured relative to the solar photospheric values of Anders & Grevesse (1989), in which $\text{Fe}/\text{H} = 4.68 \times 10^{-5}$ by number. Galactic photoelectric absorption was incorporated using the `wabs` model (Morrison & McCammon 1983); the Galactic column of absorbing material in this line of sight is $N_H = 4.58 \times 10^{20} \text{ cm}^{-2}$ (Dickey & Lockman 1990; *HEASARC* NH software). Spectral channels were grouped to have at least 25 counts/channel. Energy ranges were restricted to 0.8–10 keV for the GIS and 0.4–10 keV for the SIS. The minimum sizes for regions of spectral extraction (circular radii or annular widths) were typically 3' for the GIS and 2' for the SIS. To maximize the statistical significance of any gradients, we also assessed larger regions in the outer parts. A central 2' radius region of the GIS data was also analyzed for closer comparison with the SIS. The intracluster gas temperature in Abell 496 is cool enough (~ 4 keV) that the energy dependence of *ASCA*'s point spread function does not affect our results significantly. We first describe the results for the GIS and SIS data independently, then we describe their joint analysis.

3. Results

3.1. Temperature and Abundance Profiles

GIS spectra were extracted from regions as small as $3'$ at various distances from the cluster center. Thermal emission models (`mekal`) with variable temperatures, overall abundances, normalizations and absorbing column densities (`wabs`) were then jointly fit to GIS 2 & 3 spectra from each region. The normalizations for the GIS 2 & 3 spectra were allowed to vary independently, in order to compensate for small calibration and spatial extraction differences between the two detectors; the normalizations differ by $< 10\%$ in practice. The resulting fits were all excellent, having reduced χ^2 of $\chi^2_\nu \approx 1$. Figure 1a shows the GIS 2 & 3 spectra from central ($0 - 2'$) and outer ($3 - 12'$) regions, along with the best-fitting isothermal model. Figure 2a shows the temperature distribution derived from GIS 2 & 3 spectra, with various radial binnings; the indicated errors are 90% confidence limits. There is a very clear temperature gradient, with a temperature of $3.5^{+0.1}_{-0.1}$ keV within $0 - 3'$, while the outer regions are roughly isothermal at $\sim 4.3^{+0.1}_{-0.1}$ keV. Figure 2b shows the corresponding abundance distribution; Within the $0 - 3'$ region, the abundance is $0.52^{+0.06}_{-0.06}$ solar, which is significantly greater than that in the outer parts, $0.38^{+0.04}_{-0.04}$ solar, at a confidence level of $> 90\%$. These results are listed in Table 2.

The SIS instruments have somewhat better spatial resolution than the GIS, so for SIS data we used region sizes as small as $2'$. Fitting the same type of spectral models as before to data from SIS 0 & 1, we again found excellent fits, with $\chi^2_\nu \approx 1$. Figure 1b shows the SIS 0 & 1 spectra from the central and outer regions, along with the best-fitting isothermal model. The temperature and abundance distributions are illustrated in Figures 3a and 3b, respectively and details are listed in Table 2. The temperature is $3.1^{+0.1}_{-0.1}$ keV within the central $2'$ and rises steadily outward to $6'$ ($\sim 350 h_{50}^{-1}$ kpc), beyond which it is isothermal at $4.5^{+0.2}_{-0.2}$ keV. There is a significant spatially resolved central abundance enhancement within $4'$ (~ 230 kpc): the overall abundance within $2'$ is $0.48^{+0.06}_{-0.05}$ solar and it declines outward to $0.26^{+0.07}_{-0.06}$ solar by $6'$. These SIS results are consistent with those from the GIS.

We also jointly fitted thermal models to spectra from all four ASCA instruments, in order to reduce the fitting errors. The resulting fits had $\chi^2_\nu \approx 1$ and the temperature and abundance distributions are shown in Figures 4a & b and Table 2. The temperature rises from $3.24^{+0.07}_{-0.06}$ keV within $2'$ to $4.40^{+0.13}_{-0.13}$ keV beyond $5'$. The central abundance is $0.53^{+0.04}_{-0.04}$ solar, falling to $0.36^{+0.03}_{-0.03}$ in the outer $3-12'$ region. In this combined data set, the central abundance enhancement within $3'$ is significant at a confidence level of $\sim 99\%$. Confidence contours for the abundances in the two innermost regions are shown in Figure 5. We also used the F -test to assess the significance of the central abundance enhancement.

We simultaneously fitted the spectra from the inner and outer regions, allowing their normalizations, temperatures and abundances to vary independently. We then refit the spectra with the abundances from the two regions tied together. The χ^2 of these latter fits were larger by ≥ 26 for an increase of only one degree of freedom. The F -test indicates that the central abundance enhancement is significant at a level of $>99.99\%$.

Since there is a strong cooling flow at the center of Abell 496, we tested whether the abundance gradient described above is an artifact of our choice of spectral model. We added a cooling flow component to the `mekal` thermal emission model in the central region. The cooling flow spectral model `cflow` in XSPEC is characterized by maximum and minimum temperatures, an abundance, a slope which parameterizes the temperature distribution of emission measures, and a normalization which is simply the cooling accretion rate. We adopted the emission measure temperature distribution that corresponds to isobaric cooling flows (zero slope). We tied the maximum temperature of the cooling flow to the temperature of the thermal component, and we fixed the minimum temperature at 0.1 keV. We applied a single (but variable) global absorption to both spectral components and associated an additional, intrinsic absorption component with the cooling flow, placing it at the redshift of the cluster. The addition of the cooling flow component does not significantly affect our results for the central region: the central abundance enhancement remains significant at a confidence level of $>90\%$. The two component fits at the center are slightly worse than the isothermal model fits above, but they still have $\chi^2_\nu \approx 1$ (see Table 2). In order to apply the F -test to these cooling flow model fits, we also simultaneously fit the spectra from inner and outer regions, first allowing the abundances in the respective regions to vary independently, then tying the abundances together. The χ^2 of the fits which were forced to have identical abundances in both regions were increased by 30 relative to those which allowed a spatial gradient in abundances, for an increase of one degree of freedom; the F -test implies that the abundance gradient is significant at the $>99.99\%$ level.

3.2. Individual Elemental Abundances & Abundance Ratios

We also determined the abundances of individual elements using the `vmekal` spectral model in XSPEC. A similar analysis for the outer regions ($> 3'$) of Abell 496 was done by Mushotzky et al. (1996), whose individual elemental abundance measures are consistent with our results at the 90% confidence level. In our spectral model fits, the He abundance was fixed at the solar value, while C and N were fixed at 0.3 solar (since *ASCA* is rather insensitive to C and N and the derived abundances of other elements are not affected by the particular choice for C and N abundances). Our observed abundances are shown in Table 3

for various spatial regions.

Table 3 shows that the iron abundance is best determined and increases $\sim 50\%$ from 0.36 ± 0.03 solar in the outer parts ($> 3'$) to a central value of 0.54 ± 0.05 solar. The sulfur abundance also shows a significant gradient, rising from 0.22 ± 0.17 solar beyond $3'$ to 0.60 ± 0.2 solar at the center. The silicon abundance is $\sim 0.8 \pm 0.2$ solar, showing no significant gradient within its 90% confidence limits. The best fitting neon abundance is also nearly solar, showing no significant gradient, while the best fitting nickel abundance is ~ 2.5 times solar at the center, with a marginally significant decline to solar in the outer parts. Oxygen, magnesium, argon and calcium are poorly constrained.

Theoretical numerical models of supernovae yields predict the following elemental ratios relative to solar values: for SN Ia, the W7 model of Nomoto, Thielemann & Yokoi (1984), as updated in Nomoto et al. (1997a), gives

$$\text{O} \approx \text{Mg} \approx 0.035\text{Fe},$$

$$\text{Ne} \approx 0.006\text{Fe},$$

$$\text{Si} \approx \text{S} \approx \text{Ar} \approx \text{Ca} \approx 0.5\text{Fe},$$

$$\text{Ni} \approx 4.8\text{Fe};$$

while for SN II, Nomoto et al. (1997b) find

$$\text{O} \approx \text{Mg} \approx \text{Si} \approx 3.7\text{Fe},$$

$$\text{Ne} \approx \text{S} \approx 2.5\text{Fe},$$

$$\text{Ar} \approx \text{Ca} \approx \text{Ni} \approx 1.7\text{Fe},$$

after integrating their yields over a Salpeter mass function with upper and lower mass limits of 10 and 50 M_{\odot} , respectively.

Various observed abundance ratios within inner and outer spatial regions are shown in Table 4, along with the theoretical expectations for SN Ia and SN II ejecta; the errors associated with the observed abundance ratios are the propagated 1σ errors. Note that several abundance ratios lie significantly outside their theoretical ranges: Ne/Si ($0 - 3'$), Ne/S ($3 - 12'$) and Si/S ($3 - 12'$). Three abundance ratios show marginally significant gradients: Si/S, Si/Ni, and S/Fe.

4. Distinguishing the Relative Contributions from SN Ia & SN II

We will use the observed abundance ratios (normalized by their solar values) in Table 4 to estimate the relative contribution of SN Ia and SN II to the metal enrichment of the intracluster gas. Such estimates are complicated by uncertainties in both the observations and the theoretical yields. The yield relations above show that the most discriminatory abundance ratios are the ones involving oxygen, magnesium and neon, since their ratios to iron are 2-3 orders of magnitude smaller for SN Ia than for SN II; of these, magnesium is poorly determined, which leaves oxygen and neon. Despite their large fractional uncertainties, the fact that the observed O/Fe and Ne/Fe ratios are of order unity (see Table 4) clearly indicates the presence of SN II ejecta — these ratios are predicted to be less than a few percent for SN Ia ejecta. The 90% errors in these abundance ratios are not so large that they can be consistent with SN Ia ejecta alone. On the other hand, the observed O/Fe and Ne/Fe ratios are about half the values predicted for pure SN II ejecta, which may indicate dilution by SN Ia ejecta. The SN Ia iron mass fractions indicated by these abundance ratios are indicated in Table 4. However, the theoretical iron yields from SN II are uncertain by a factor of ~ 2 (Woosley & Weaver 1995; Arnett 1996; Gibson et al. 1997), so this systematic uncertainty obscures the relative contribution from SN Ia and SN II.

The abundance ratios with the smallest fractional errors are Si/Fe, S/Fe and Ni/Fe. The Si/Fe and Ni/Fe ratios in Table 4 indicate a roughly comparable mix of SN II and SN Ia ejecta in the outer parts, while the SN Ia/II mix indicated by the S/Fe ratio is inconsistent with those derived from the Si/Fe and Ni/Fe ratios (we show below that elemental ratios involving sulfur are problematic). The associated SN Ia iron mass fractions are listed in Table 4 for these ratios as well. These three abundance ratios also involve iron, the production of which in SN II models is uncertain by a factor of ~ 2 , so we next consider SN Ia/II discriminators that do not involve iron.

Two well-determined ratios independent of iron are Si/Ni and Si/S. The SN Ia/II ratio derived from Si/Ni is consistent with the values derived above (see Table 4), indicating that SN Ia contribute 74% (65%) of the iron mass in the inner $0 - 2'$ ($0 - 3'$) region and 46% in the outer $3 - 12'$ region. However, the best-fit value of the Si/S ratio is outside the theoretical boundaries in the outer parts of Abell 496, although its errors are large enough to be consistent with the expectation for SN II ejecta. Inspection of Table 4 shows that most of the best fit values of the other ratios involving sulfur in the outer parts are also systematically outside the theoretical range. We conclude, despite the large fractional errors, that sulfur is likely to be overproduced in the SN II models we have adopted. To be consistent with the results from the other elemental ratios above, sulfur production in SNe II should be reduced by a factor of $\sim 2-4$ relative to the models of Nomoto et al. (1997b).

Figure 6 compares the confidence contours of silicon and sulfur in the innermost and outermost regions. The solid straight lines correspond to the theoretical Si/S predictions for pure SN Ia and SN II ejecta, with the SN II value “corrected” by a factor of 3.8; the dashed straight line is the uncorrected value for SN II. This overproduction of sulfur in other SN II models was noted previously by Mushotzky et al. (1996), Loewenstein & Mushotzky (1996) and Gibson et al. (1997). Recently, Nagataki & Sato (1998) found that this sulfur discrepancy was reduced when they used the theoretical SN II yields of Nagataki et al. (1998), who explored the affects of asymmetric explosions.

Figure 7 summarizes our estimates of the iron mass fraction from SN Ia, as derived from the variety of elemental abundance ratios described above; values for the inner $0 - 2'$ region are indicated by filled circles, while empty circles correspond to $3 - 12'$. If the outer region is more dominated by SN II and the central region is dominated by SN Ia, then the filled and empty symbols should be segregated. Such segregation is obvious, despite the large individual errors, and the consistency of the results for ratios not involving sulfur is particularly noteworthy. In Figure 7 the average theoretical yield of sulfur from SN II has been reduced by a factor of 3.8; the estimates from sulfur ratios are consequently more in line with the other estimates.

For our consensus estimate of the iron mass fraction due to SN Ia, we average the SN Ia iron mass fractions for five of the seven ratios discussed above: O/Fe, Ne/Fe, Si/Fe, Ni/Fe and Si/Ni (the two ratios involving sulfur are excluded). Our best estimates for the SN Ia iron mass fraction are $72 \pm 11\%$ within $0 - 2'$, $65 \pm 12\%$ within $0 - 3'$, and $46 \pm 17\%$ within $3 - 12'$ (these values are denoted as μ in Figure 7). Although the exact proportions of SN Ia and SN II ejecta are sensitive to our adopted theoretical SN II yields, this constitutes marginal evidence for an increase in the proportion of iron from SN Ia at the center relative to the outer parts. For our adopted yields, the proportion of iron from SN Ia is $\sim 50\%$ larger at the center than the outer parts. This increased proportion of SN Ia ejecta at the center is such that the central iron abundance enhancement can be attributed wholly to SN Ia. In comparing the theoretical yields for SN Ia and SN II in §3.2, it is apparent that if there is an iron abundance gradient due to an increase in the proportion of iron from SN Ia, the next most likely elements to exhibit detectable gradients should be nickel and sulfur, as we indeed observe. Combining our results for the gradients in iron abundance and the relative proportion of SN Ia and II, we find that the iron abundance due to SN II is $A_{\text{FeSNII}} = 0.19 \pm 0.06$ solar in the outer parts ($3 - 12'$) and 0.15 ± 0.06 solar near the center ($0 - 2'$), exhibiting no significant gradient. The iron abundance due to SN Ia is $A_{\text{FeSNIa}} = 0.17 \pm 0.06$ solar in the outer parts, increasing a factor of ~ 2 to 0.38 ± 0.07 solar near the center (see Table 5).

5. Distinguishing between Possible Metal Enrichment Mechanisms

We showed above that iron, nickel and sulfur abundances are centrally enhanced in Abell 496 and that gradients in various elemental ratios indicated that these central abundance enhancements are largely due to SN Ia ejecta. Our more model dependent result is that nearly $\sim 50\%$ of the iron $3 - 12'$ from the cluster center comes from SN Ia. We will first distinguish between several possible mechanisms for producing central abundance enhancements in the cluster. Then we will assess the relative roles of winds and ram pressure stripping as metal enrichment mechanisms for the bulk of the cluster.

5.1. Mechanisms for Creating Central Abundance Enhancements

In the Introduction we identified several mechanisms which may cause central abundance enhancements in intracluster gas: 1) the spatial density of metal-injecting galaxies tends to decline more rapidly with radius than does the intracluster gas density, so the gas may be more contaminated at the center; 2) ram pressure stripping of the metal-rich gas in cluster galaxies by intracluster gas is more effective at the center, where the intracluster gas density is highest; 3) secular (post-wind) mass loss from the stars in central dominant galaxies may accumulate near the cluster center; 4) if early-type galaxies blew proto-galactic winds, such winds may be at least partially suppressed in central dominant galaxies, by virtue of their location at the bottom of their clusters' gravitational potentials and in the midst of the highest intracluster gas density. We will consider each of these mechanisms in turn.

Since the central abundance enhancements Abell 496 are also associated with gradients in elemental abundance *ratios*, the central abundance enhancements in *cannot* be due to the density of metal-ejecting galaxies falling more quickly with radius than the intracluster gas density: in this case the abundances would decline with radius, but the proportion of SN Ia and SN II ejecta would remain constant.

The remaining three mechanisms can in principle produce spatial gradients in the proportion of SN Ia/II ejecta. To help differentiate between them, we will compare the iron mass to optical light ratio (Renzini et al. 1993) in the vicinity of the cD to that of the cluster as a whole. This calculation will contribute to an argument against ram pressure stripping being the cause of the central abundance enhancements. To assess whether accumulated stellar mass loss can cause the central enhancement, we will compare the gaseous iron production and retention of the cD to those of a more isolated X-ray luminous elliptical galaxy. For the cD, we will separately consider the iron from SN Ia and SN II and we will

treat the iron from SN Ia in two ways: we will first attribute to the cD all the SN Ia iron in the central region where the abundance is enhanced; however, this may be an overestimate, since the cD’s central location makes it difficult to separate general intracluster gas from its own interstellar medium, even if it is substantial. Consequently, we will also consider the possibility that only the “excess” iron at the center (that which gives rise to the central abundance enhancement and to the central change in elemental abundance ratios) was generated by the cD. This “excess” is one third of all the iron within $3'$, or half of the iron attributable SN Ia.

We derived the intracluster gas density distribution in Abell 496 using *Einstein* data to determine the shape (core radius and asymptotic slope of a β -model) of its X-ray surface brightness distribution and using the *ASCA* observations described in §2 to provide the flux normalization. Given the iron abundances listed in Table 3, we calculated the iron mass within the spherical volume contained between $0 - 3'$ to be $M_{\text{Fe}} \approx 5.1 \times 10^9 M_{\odot}$, as listed in Table 5 (also listed are calculations for $0 - 2'$). Using our best estimate of the SN Ia iron mass fraction described in §4, we calculated the iron mass from SN Ia to be $M_{\text{FeSN Ia}} \approx 3.2 \times 10^9 M_{\odot}$ within $0 - 3'$.

We derived the galaxies’ optical luminosity distribution in Abell 496 from the galaxy morphological and (*V*-band) photometric data of Dressler (1980). We assumed that early-type galaxies are the source of the intracluster iron (cf. Arnaud et al. 1992) and derived their cumulative spherical luminosity distribution from a deprojection of their cumulative surface luminosity distribution. We converted the Dressler (1980) *V* magnitudes to *B* by assuming $B - V = 1$ for early-type galaxies. For the central cD, we used the photometry of Valentijn (1983), which assigns a total *B* magnitude of $B_T = 13.42$, giving a blue luminosity of $L_B = 2.6 \times 10^{11} h_{50}^{-2} L_{\odot}$. We distributed the luminosity of the cD over several radial bins, using an $r^{1/4}$ law with the same effective radius, to avoid an artificial luminosity spike at the center. Table 5 lists the iron mass to optical light ratio for SN Ia and II ejecta within various projected regions, $0-2'$, $0-3'$ and $3-12'$. The errors shown in Table 5 include the iron mass and luminosity errors; the fitting errors from the luminosity deprojection procedure are relatively small, so are not included.

It can be seen from Table 5 that the iron mass to light ratio for SN II ejecta is $\sim 2-6$ times smaller at the center than in the outer regions. If ellipticals had protogalactic winds driven by SN II, this shows that such a wind in the cD was not suppressed by it being at the cluster center (i.e. by being at the bottom of the gravitational potential well of the cluster and in the midst of the highest intracluster gas density). Given that we see no significant gradient in SN II ejecta (see §4), this suggests that the SN II ejecta in vicinity of the cD is simply the result of a fairly uniformly mixed contamination in the cluster (in

the regions observed). The nominal SN Ia iron mass to light ratio in the central region is somewhat less than that of the outer parts, but the associated errors are large enough that this difference is not significant. The iron mass to light ratios in the outer parts are indicative of what early-type galaxies actually ejected in the course of their lives, so it is clear that the *total* iron production and ejection per unit luminosity in the cluster exceeds what is seen in the immediate vicinity of the cD. We list in Table 5 the average supernovae rates required to generate the intracluster iron in each region, as derived from the listed iron mass to luminosity ratios. The supernova rates are given in SNU (where 1 SNU is one supernova per $10^{10} L_{B\odot}$ per 100 yrs) and we assumed that the ejection occurred over 10^{10} yrs and adopted average ejected iron masses per supernova of $0.74 M_{\odot}$ for SN Ia (Nomoto et al. 1997a) and $0.091 M_{\odot}$ for SN II (Nomoto et al. 1997b).

If ram pressure stripping is the primary source of SN Ia material at the center of the cluster, the cD is the one galaxy in the cluster which should not be stripped. Therefore the cD should exhibit its accumulated history of SN Ia ejecta, in addition to any ejecta stripped from other galaxies as they passed near the cluster center. The cD should then have more SN Ia iron than expected for its luminosity. We showed above that the cD, if anything, has less than expected (see Table 5). However, it could be that much of its accumulated stellar mass loss was overwhelmed and advected inward with the cluster cooling flow (perhaps to condense out and form stars), which has an accretion rate of $\dot{M} \approx 100 - 200 M_{\odot} \text{ yr}^{-1}$.

There are at least three additional reasons why ram pressure stripping is unlikely to be the source of SN Ia iron at the center of the cluster. First, the gaseous abundances measured in most early-type galaxies by *ASCA* (Loewenstein et al. 1994; Matsumoto et al. 1997) and *ROSAT* (Davis & White 1996) are 0.2-0.4 solar, significantly less than the 0.5-0.6 solar abundance observed at the cluster center. Only the most luminous ellipticals, which also tend to be at the centers of galaxy clusters or groups, are observed to have gaseous abundances of 0.5-1 solar. Second, gaseous abundances in ellipticals tend to decline outward from their centers, as observed in NGC 4636 (Matsushita et al. 1997) and other early-type galaxies (Matsushita 1997), since the mass-losing stars in ellipticals exhibit such metallicity gradients; thus, most stripped gas will have even lower abundances than indicated by the global X-ray measures of ellipticals (since global measures are weighted by centrally concentrated emission measures in ellipticals), which are already too low. Third, since the efficiency of ram pressure stripping depends on the intracluster gas density, which declines strongly with radius, the abundances of SN Ia ejecta should also decline strongly with radius, which is not observed; we see only a factor of two decline in the iron abundance from SN Ia (see Table 5). We conclude that ram pressure stripping is not the cause of the central abundance enhancements in Abell 496. If ram pressure stripping is effective in the cluster, it would act to *dilute* the central abundance enhancement.

We will now use X-ray observations of an individual elliptical to see how much gaseous iron it has accumulated per unit optical luminosity and compare with the cD. NGC 4636 is a particularly X-ray luminous elliptical for its optical luminosity, 10° from the center of the Virgo cluster in the Virgo Southern Extension (Nolthenius 1993). Its metric X-ray to optical luminosity ratio is ~ 5 times larger than the median for ellipticals (White & Davis 1999), indicating that it has been particularly successful in retaining its hot gas. Matsushita et al. (1998) suggest that NGC 4636 may even be at the center of a small group of galaxies, with its emission enhanced by group gas. If this is true, it makes our pending conclusion even stronger. The optical and X-ray luminosities of NGC 4636 are $L_B \approx 3 \times 10^{10} L_\odot$ and $L_X \approx 4 \times 10^{41} \text{ erg s}^{-1}$, adopting a distance of 17 Mpc. Very deep ASCA exposures of this galaxy have been analyzed by Matsushita et al. (1997; 1998), who found an abundance gradient characterized by a central value of ~ 0.65 solar (converted to the photospheric abundance scale), declining to ~ 0.2 solar $10'$ away.

We used the gas distribution of Matsushita et al. (1998) and the abundance distribution of Matsushita et al. (1997) to calculate the iron mass within $7r_{\text{eff}}$ in NGC 4636. This encompasses the bulk of its iron content and virtually all of its optical light. We compare this to the iron mass and optical luminosity within $3'$ of the center of Abell 496, which encompasses most of the region with enhanced abundances (see Figure 3b). We find that the SN Ia iron mass to luminosity ratio for the cD is ~ 40 times greater than in NGC 4636. If we attribute to the cD only the “excess” amount of SN Ia iron at the center compared to the rest of the cluster, the SN Ia iron mass to light ratio in the cD is still ~ 20 times higher than within NGC 4636. The discrepancy is actually even greater than indicated, since we have overestimated the SN Ia iron within NGC 4636 by assuming that all of its iron was produced by SN Ia and we have underestimated the SN Ia iron in the vicinity of the cD by restricting ourselves to within $3'$, while the SIS data show that abundances are enhanced out to $\sim 5'$.

Thus, the central abundance enhancements in Abell 496 are not likely to be due to secularly accumulated stellar mass loss in the cD (that is, mass loss accumulated since a putative protogalactic wind phase). The iron mass to luminosity ratio in the vicinity of the cD is much larger than in even the most X-ray luminous isolated ellipticals. This discrepancy cannot be explained by insisting that NGC 4636 has already been stripped; it is one of the most X-ray luminous ellipticals and is not in the midst of a cluster environment. It is therefore not in an environment in which it is likely to be stripped and it may actually be at the center of its own group (Matsushita et al. 1998). Furthermore, we have already shown that ram pressure stripping is not a tenable cause of the abundance enhancements at the center, where ram pressure should be most effective. Thus, the cD in Abell 496 is spatially associated with much more iron per unit luminosity than more isolated luminous

ellipticals. This iron concentration has developed in spite of the advective action of the cluster cooling flow, which has an accretion rate which is two orders of magnitude greater than the current mass loss rate in the cD, (which should be several solar masses per year, given its optical luminosity).

We propose that the central gradients in abundances and abundance ratios in Abell 496 result from a partially suppressed SN Ia-driven wind from the cD. This would be a secondary wind phase, following a more vigorous, unsuppressed protogalactic wind driven by SN II. Such a secondary wind phase in noncentral early-type galaxies can also generate the SN Ia enrichment seen in the bulk of the intracluster gas, as we argue in the next subsection. As we showed above, the SN II iron mass to light ratio in the vicinity of the cD and the lack of a central enhancement in SN II ejecta indicate that it lost the bulk of its SN II ejecta. However, a weaker SN Ia-driven wind would be more readily suppressed at center of the cluster, due to the depth of the gravitational potential and the high ambient intracluster gas density. SN Ia-driven winds would be expected to be less vigorous than the initial SN II-driven winds, since SN Ia inject ~ 10 times less energy per unit iron mass than SN II, and the observations indicate that comparable amounts of iron came from SN Ia and SN II. Therefore, SN II inject ~ 10 times more energy into intracluster gas than SN Ia, and the timescale associated with SN II-dominated phase is likely to be much shorter than for the SN Ia-dominated phase.

5.2. Global Enrichment Mechanisms

As mentioned in the introduction, the two metal enrichment mechanisms usually considered for the bulk of intracluster gas are protogalactic winds from early-type galaxies and ram pressure stripping of gas from galaxies in the cluster. Recent *ASCA* spectroscopy (Mushotzky & Loewenstein 1997; Mushotzky et al. 1996) showed that global intracluster metal abundances are consistent with ejecta from SN II, which supports the protogalactic wind model. However, theoretical uncertainties about the elemental yields from Type II supernovae make it difficult to determine confidently the relative proportion of iron from SN II and SN Ia in intracluster gas (Gibson et al. 1997). The SN II models that we have adopted (Nomoto et al. 1997b) in this work lead us to conclude that nearly 50% of the iron in Abell 496 comes from SN Ia. Similar conclusions were reached for other clusters by Ishimaru & Arimoto (1997) and Nagataki & Sato (1998), who used different theoretical models for SN II. If this large proportion of SN Ia iron in clusters is a robust observation, it remains to be determined whether it is from ram pressure stripping or galactic winds.

As mentioned in the previous subsection, the gaseous abundances measured in most

early-type galaxies by *ASCA* and *ROSAT* are 0.2-0.4 solar. While such abundances are substantially less than that observed in the center of Abell 496, they are more comparable to the abundances observed in the outer parts of the cluster. However, as noted in the previous subsection, the gaseous abundances in ellipticals tend to decline outward from their centers, so most stripped gas would have lower abundances than indicated by the centrally-weighted global X-ray measures of ellipticals. Furthermore, if ram pressure stripping is effective in the outer parts of the cluster, it should be even more effective at the center, where the intracluster gas density is highest. However, we showed in the previous subsection that ram pressure stripping cannot account for the central concentration of metals. Renzini et al. (1993) have also argued strongly against ram pressure stripping being very significant in clusters, citing the lack of a strong metallicity trend with cluster temperature: hot clusters have higher velocity dispersions and tend to have much higher gas densities than cool clusters, so ram pressure stripping should be much more effective in hot clusters than cool clusters. The lack of a strong metallicity trend with cluster temperature implies that ram pressure is not the major source of intracluster metals. We also conclude that ram pressure stripping is not the dominant source of metals in intracluster gas. Ram pressure stripping could very well be acting, but it would tend to *dilute* intracluster abundances, particularly near the center.

We propose instead that the bulk of intracluster gas is contaminated by two phases of winds from early-type galaxies: an initial SN II-driven protogalactic wind phase, followed by a secondary, less vigorous SN Ia-driven wind phase. As mentioned in the previous subsection, secondary SN Ia-driven winds would be less vigorous than the initial SN II-driven protogalactic winds since SN Ia inject ~ 10 times less energy per unit iron mass than SN II, and the observations indicate that comparable amounts of iron came from SN Ia and SN II. Fukazawa et al. (1998) recently invoked SN II-driven protogalactic winds to account for their *ASCA* measures of Si/Fe ratios in 40 clusters; their measured Si/Fe ratios were lower in cool clusters than hot clusters. Lower Si/Fe ratios imply a greater fraction of SN Ia ejecta (see §3.2), so Fukazawa et al. (1998) suggested that SN II-driven protogalactic winds were energetic enough that SN II-enriched material was able to escape cool clusters, which have shallower gravitational potentials than hot clusters. Davis, Mulchaey & Mushotzky (1998) recently showed that this trend continues down to galaxy groups. Less vigorous secondary SN Ia-driven winds would allow SN Ia-enriched material to escape most galaxies, but not clusters. Weaker winds could be partially suppressed in a cD galaxy, due to its location at the bottom of the clusters' gravitational potential and in the midst of the highest ambient intracluster gas density.

As mentioned above, we find that the relative enrichment by SN Ia and SN II is comparable by mass. Fukazawa et al. (1998) note that the very fact that they observed a

correlation of the Si/Fe ratio with cluster temperature indicates that there must be roughly comparable amounts of iron from SN Ia and SN II in typical clusters; if either SN Ia or SN II ejecta dominated the ejecta, a trend in a mere trace of the other SN type would not be able to induce such a trend in the global measures of Si/Fe. Thus, Fukazawa et al. (1998) insist that the SN Ia/II mixture in clusters cannot be as ambiguous as suggested by Gibson et al. (1997).

If suppressed winds are the cause of central abundance enhancements in other clusters, the prevalence of such enhancements in cooler clusters may be related to their cooling flow properties. Cool clusters tend to have cooling flows with smaller accretion rates than hot clusters, so the history of prior metal ejection from the central cD may be more likely to survive in cool clusters. For a given cD optical luminosity, the metal ejection is more likely to extend beyond the cooling flow region (since the central intracluster gas density is smaller in cool clusters than hot clusters), and the inward advection of the cooling flows would be less destructive to preexisting abundance gradients than in hotter clusters with higher accretion rates.

The picture we are proposing has not been explicitly modeled to date. Some previous evolutionary models for the gas in ellipticals have presumed the existence of an initial SN II-driven wind, without modeling it, and concentrated on a later SN Ia-drive wind phase (Loewenstein & Mathews 1991; Ciotti et al. 1991). Some of these models assume that the bulk of intracluster iron comes from SN Ia. Others investigators have assumed that the bulk of intracluster iron comes from SN II and model only SN II-driven protogalactic winds in detail (Larson & Dinerstein 1975; David et al. 1991). However, in all recent investigations, present epoch SN Ia rates were adopted which lead to huge overpredictions of the current gaseous abundances in ellipticals: iron abundances were theoretically predicted to be 3-5 times solar, while *ASCA* and *ROSAT* observations find abundances to be 0.1-1 solar.

In parlance similar to that of Renzini et al. (1993), we are proposing a wind-outflow-inflow (WOI) model in which the “wind” is driven by SN II, the less vigorous “outflow” is driven by SN Ia, and the inflow experiences much less contamination by SN Ia than in previous modeling. As mentioned before, previous evolutionary models for the gas in ellipticals (Loewenstein & Mathews 1991; Ciotti et al. 1991; David et al. 1991) tend to vastly overpredict their current atmospheric iron abundances. To generate SN Ia-enriched outflows that can contaminate intracluster gas, but leave current abundances subsolar in elliptical atmospheres, requires rather different evolution in the SN Ia rate than in previous models. Prior models of SN Ia-driven winds tend to inject roughly the right amount of iron in clusters (to within a factor of ~ 2 or so). But the SN Ia rate must decline much faster than in previous models if the current SN Ia rate must be as low as $\lesssim 0.03$ SNU (Loewenstein &

Mushotzky 1997) to match the low iron abundances in elliptical atmospheres. This rate is 3-10 times smaller than previously adopted and is ~ 4 times smaller than the most recent optical estimate of the current SN Ia rate in ellipticals (0.13 SNU; Capellaro et al. 1997). To generate the amount of SN Ia observed in intracluster gas, the SN Ia rate at earlier times must be much larger than previously modeled, to compensate for the much lower current rate. These heuristic constraints on the evolution of the SN Ia rate are not yet theoretically motivated.

6. Summary

We have carried out a detailed analysis of the distribution of elemental abundances in the intracluster gas of Abell 496. Our main results which are independent of our choice of supernovae yield models are:

1. The hot gas of Abell 496 has significant abundance gradients: the iron abundance 3–12' from the center is $0.36_{-0.03}^{+0.03}$ solar and it rises by 50% to $0.53_{-0.04}^{+0.04}$ solar within 2'; nickel and sulfur also have significant central concentrations.
2. There is marginal evidence of spatial gradients in elemental *ratios* in this cluster.
3. A variety of abundance ratios individually and collectively indicate that SN Ia ejecta is more dominant in the center than in the outer parts.
4. We find no significant gradient in SN II ejecta.
5. In the vicinity of the central cD, the iron mass to light ratio for iron from SN II is significantly lower than in the outer regions, showing that any protogalactic wind from the cD was not suppressed by the cD being at the bottom of the cluster's gravitational potential well.
6. In the vicinity of the central cD, the SN Ia iron mass to light ratio is comparable to (perhaps somewhat less than) that in the outer regions, despite the central enhancement of SN Ia ejecta.
7. The existence of gradients in elemental abundance *ratios* implies that the central abundance enhancements cannot be due to the density of metal-ejecting galaxies falling more quickly with radius than the intracluster gas.
8. Ram pressure stripping is unlikely to generate the observed central abundance enhancements, since the gaseous abundances observed in elliptical atmospheres tend

to be substantially less than the abundances observed in the intracluster gas near the center.

9. A two stage galactic wind model, SN II-driven protogalactic winds followed by less energetic SN Ia-driven outflows, is proposed to generate comparable levels (by mass) of iron contamination by SN Ia and SN II in the intracluster gas of Abell 496.
10. The less energetic secondary SN Ia-driven winds are more likely to be suppressed in the central cD, due to its position at the bottom of the gravitational potential and in the midst of the highest intracluster gas density; such a suppressed wind from the cD may generate the observed central abundance enhancements.

Results which are more dependent upon our particular choice of supernovae yield models include:

1. SN Ia account for $\sim 46\%$ of the iron mass $3 - 12'$ from the center of the cluster and $\sim 72\%$ of the iron mass within $2'$.
2. The central iron abundance enhancement can be attributed wholly to the iron associated with the central enhancement of SN Ia ejecta.
3. The analysis of several elemental abundance ratios indicates that sulfur is consistently overproduced in theoretical SN II models by a factor of $\sim 2-4$, as previously noted by Mushotzky et al. (1996), Loewenstein & Mushotzky (1996) and Gibson et al. (1997); however, Nagataki & Sato (1998) find that the sulfur discrepancy is reduced when they employ the SN II yields of Nagataki et al. (1998).

While our confirmation of centrally enhanced abundances in Abell 496 is robust, our detection of gradients in abundance ratios is more marginal. Multiple element ratios had to be assessed simultaneously to improve the statistical errors. Our scheduled *Chandra* observation of Abell 496, should allow us to assess more easily the nature of gradients in abundances and abundance ratios, given the higher spatial resolution and relative lack of scattering compared to *ASCA*. Since our suggested mechanism for generating the gradients in abundances and abundance ratios should not be specific to just one cluster, we will be applying similar analyses to *ASCA* data for other clusters, as well.

This work was partially supported by the NSF and the State of Alabama through EPSCoR grant EHR-9108761. REW also acknowledges partial support from NASA grant NAG 5-2574. This research made use of the HEASARC *ASCA* database and NED.

REFERENCES

- Allen, S. W. 1997, MNRAS, preprint
- Anders, E. & Grevesse N. 1989, *Geochimica et Cosmochimica Acta*, 53, 197
- Arnaud, K. A. 1996, in *Astronomical Data Analysis Software and Systems V*, ASP Conf. Series volume 101, eds. Jacoby, G. & Barnes, J., p.17
- Arnaud, K. A., Mushotzky, R. F., Ezawa, H., Fukazawa, Y., Ohashi, T., Bautz, M. W., Crewe, G. B., Gendreau, K. C., Yamashita, K., Kamata, Y., Akimoto, F. 1994, ApJ, 436, L67
- Arnaud, M., Rothenflug, R., Boulade, O., Vigroux, L. & Vangioni-Flam, E. 1992, A&A, 254, 49
- Arnett, D. 1996, *Supernovae and Nucleosynthesis* (Princeton: Princeton Univ. Press)
- Bird, C. M. 1993, PhD thesis
- Canizares, C. R., Markert, T. H., & Donahue, M. E. 1988, in *Cooling flows in clusters and galaxies*, ed. A. C. Fabian (Dordrecht: Kluwer), p. 63
- Canizares, C. R.; Clark, G. W.; Jernigan, J. G.; Markert, T. H. 1982, ApJ, 262, 33
- Cappellaro, E., Turatto, M., Tsvetkov, D. Yu., Barttunov, O. S., Pollas, C., Evans, R., Hamuy, M. 1997, A&A, 322, 431
- Ciotti, L., Pellegrini, S., Renzini, A., D’Ercole, A. 1991, ApJ, 376, 380
- Cowie, L. L., Hu, E. M., Jenkins, E. B. & York, D. G. 1983, ApJ, 272, 29
- Dickey, J. & Lockman, F. J. 1990, ARA&A, 28, 215
- David, L. P., Forman, W., & Jones, C. 1990, ApJ, 359, 29
- Dressler, A. 1980, ApJS, 42, 565
- Davis, D. S., Mulchaey, J. S. & Mushotzky, R. F. 1998, astro-ph/9808085
- Davis, D. S. & White, R. E. III 1996, ApJ, 470, L35
- Dupke, R. A. & White, R. E. III 1999, in preparation
- Edge, A. C., Stewart, G. C. & Fabian, A. C. 1992, MNRAS, 258, 177
- Ezawa, H., Fukazawa, Y., Makishima, K., Ohashi, T., Takahara, F., Xu, H., Yamasaki, N. Y. 1997, ApJ, 490, L33
- Faber, S. M., Wegner, G., Burstein, D., Davies, R. L., Dressler, A., Lynden-Bell, D., Terlevich, R. J., 1989, ApJS, 69, 763

- Fukazawa, Y., Ohashi, T., Fabian, A. C., Canizares, C. R., Ikebe, Y., Makishima, K., Mushotzky, R. F. & Yamashita, K. 1994, PASJ, 46, L55
- Gibson, B. K. 1997, MNRAS, 290, 471
- Gibson, B. K., Loewenstein, M. & Mushotzky, R. F. 1997, MNRAS, 290, 623
- Gunn, J. E. & Gott, J. R. III 1972, ApJ, 176, 1
- Heckman, T. M. 1981, ApJ, 250, L59
- Ikebe, Y., Makishima, K., Ezawa, H., Fukazawa, Y., Hirayama, M., Honda, H., Ishisaki, Y., Kikuchi, K., Kubo, H., Murakami, T., Ohashi, T. & Takahashi, T. 1997, ApJ, 481, 660
- Ishimaru, Y. & Arimoto, N. 1996, PASJ, 49, 1
- Kaastra, J. S. 1992, *An X-Ray Spectral Code for Optically Thin Plasmas*, (Internal SRON-Leiden Report, updated version 2.0)
- Koyama, K., Takano, S. & Tawara, Y. 1991, Nature, 350, 135
- Kowalski, M. P., Cruddace, R. G., Snyder, W. A., Fritz, G. G., Ulmer, M. P. & Fenimore, E. E. 1993, ApJ, 412, 489
- Larson, R. B. & Dinerstein, H. L. 1975, PASP, 87, 911
- Liedahl, D. A., Osterheld, A. L. & Goldstein, W. H. 1995, ApJ, 438, L115
- Loewenstein, M. & Mathews, W. G. 1991, ApJ, 373, 445
- Loewenstein, M., Mushotzky, R. F., Tamura, T., Ikebe, Y., Makishima, K., Matsushita, K., Awaki, H. & Serlemitsos, P. J. 1994, ApJ, 436, L75
- Loewenstein, M. & Mushotzky, R. F. 1996, ApJ, 466, 695
- Loewenstein, M. & Mushotzky, R. F. 1997, astro-ph/9710339
- Matsushita, K. 1997, Ph.D. thesis, University of Tokyo
- Matsushita, K., Makishima, K., Awaki, H., Canizares, C. R., Fabian, A. C., Fukazawa, Y., Loewenstein, M., Matsumoto, H., Mihara, T., Mushotzky, R. F., Ohashi, T., Ricker, G. R., Serlemitsos, P. J., Tsuru, T., Tsusaka, Y., & Yamazaki, T. 1994, ApJ436, L41
- Matsushita, K., Makishima, K., Rokutanda, E., Yamazaki, N. Y., & Ohashi, T., 1997, ApJ488, L125
- Matsushita, K., Makishima, K., Ikebe, Y., Rokutanda, E., Yamazaki, N. Y., & Ohashi, T., 1998, ApJ499, L13
- Matsushita, et al. 1997, ApJ

- Mewe, R., Gronenschild, E. H. B. M. & Van den Oord, G. H. J. 1985, *A&AS*, 62, 197
- Mewe, R., Lemen, J. R. & Van den Oord, G. H. J. 1986, *A&AS*, 65, 511
- Morrison, R. & McCammon, D. 1983, *ApJ*, 270, 119
- Mushotzky, R. F. 1984, *Phys. Scr*, T7, 157
- Mushotzky, R. F. 1995, in *New Horizons of X-ray Astronomy*, ed. Makino & T. Ohashi (Tokyo: Universal Academy), 243
- Mushotzky, R. F. & Loewenstein, M. 1997, *ApJ*, 481, L63
- Mushotzky, R. F., Loewenstein, M., Arnaud, K. A., Tamura, T., Fukazawa, Y., Matsushita, K., Kikuchi, K. & Hatsukade, I. 1996, *ApJ*, 466, 686
- Mushotzky, R. F. & Szymkowiak, A. E. 1988, in *Cooling flows in clusters and galaxies*, ed. A. C. Fabian (Dordrecht: Kluwer), p. 53-62
- Nagataki, S. & Sato, K. 1998, *ApJ*, 504, 629
- Nagataki, S., Hashimoto, M., Sato, K., Yamada, S. 1998, *ApJ*, submitted
- Nepveu, M. 1981, *A&A*, 101, 362
- Nolthenius, R. 1993, *ApJS*, 85, 1
- Nomoto, K., Iwamoto, K., Nakasato, N., Thielemann, F.-K., Brachwitz, F., Tsujimoto, T., Kubo, Y. & Kishimoto, N., 1997a, *Nuclear Physics A*, Vol. A621
- Nomoto, K., Hashimoto, M., Tsujimoto, T., Thielemann, F.-K., Kishimoto, N., & Kubo, Y. 1997b, *Nuclear Physics A*, Vol. A616
- Nomoto, K., Thielemann, F.-K. & Yokoi, K. 1984, *ApJ*, 286, 644
- Nulsen, P. E. J., Stewart, G. C., Fabian, A. C., Mushotzky, R. F., Holt, S. S., Ku, W. H.-M. & Malin, D. F. 1982, *MNRAS*, 199, 1089
- Pislar, V., Durret, F., Gerbal, D., Lima Neto, G. B. & Slezak, E. 1997, *A&A*, 322, 53
- Ponman, T. J., Bertram, D., Church, M. J., Eyles, C. J., Watt, M. P., Skinner, G. K. & Willmore, A. P. 1990, *Nature*, 347, 450
- Renzini, A., Ciotti, L., D’Ercole, A. & Pellegrini, S. 1993, *ApJ*, 419, 52
- Schombert, J. M. 1986, *ApJS*, 60, 603
- Thielemann, F.-K., Nomoto, K. & Yokoi, K. 1986, *A&A*, 158, 17
- Thomas, P. A., Fabian, A. C. & Nulsen, P. E. J. 1987, *MNRAS*, 228, 973
- Ulmer, M. P., Cruddace, R. G., Fritz, G. G., Snyder, W. A., Fenimore, E. E. 1987, *ApJ*, 319, 118

- Valentijn, E. A. 1983, A&A, 118, 123
- White, R. E. III 1991, ApJ, 367, 69
- White, R. E. III & Davis, D. S. 1997, in *Galactic & Cluster Cooling Flows*, ed. N. Soker, *A.S.P. Conf. Series Vol. 115* (San Francisco: A.S.P.) pp. 217-226
- White, R. E. III & Davis, D. S. 1999, in preparation.
- White, R. E. III, Day, C. S. R., Hatsukade, I., & Hughes, J. P. 1994, ApJ, 433, 583
- Woosley, S. E. & Weaver, T. A. 1995, ApJS, 101, 181
- Xu, H., Ezawa, H., Fukazawa, Y., Kikuchi, K., Makishima, K., Ohashi, T. & Tamura, T., 1997, PASJ, 49, 9
- Zabludoff, A., Huchra, J. P., & Geller, M. J. 1990, ApJS, 74, 1

Figure Captions

Fig. 1.— a) GIS 2 & 3 spectra for inner ($0 - 2'$) (*top*) and outer ($3 - 12'$) (*bottom*) regions; solid lines represent the best-fitting isothermal model; individual lines and line complexes are identified. b) SIS 0 & 1 spectra for inner ($0 - 2'$) (*top*) and outer ($3 - 12'$) (*bottom*) regions; solid lines represent the best-fitting isothermal model.

Fig. 2.— Results of simultaneous isothermal fits to GIS 2 & 3 data; errors are 90% confidence limits; $1' \approx 57h_{50}^{-1}$. a) Temperature (in keV) distribution; b) Abundance (relative to solar) distribution.

Fig. 3.— Results of simultaneous isothermal fits to SIS 0 & 1 data; errors are 90% confidence limits; $1' \approx 57h_{50}^{-1}$. a) Temperature (in keV) distribution; b) Abundance (relative to solar) distribution.

Fig. 4.— Results of simultaneous isothermal fits to SIS 0 & 1 and GIS 2 & 3 data. Errors are 90% confidence limits; $1' \approx 57h_{50}^{-1}$. a) Temperature (in keV) distribution; b) Abundance (relative to solar) distribution.

Fig. 5.— Confidence contours for abundances from simultaneous fits to the innermost ($0 - 2'$) and outermost ($3 - 12'$) regions of data from all four instruments. The three contours correspond to 68%, 90% and 99% confidence limits.

Fig. 6.— Confidence contours for the Si/S ratio in inner and outer regions. The solid straight lines are the theoretical Si/S ratios for SN Ia and SN II, with the latter reduced by a “correction” factor of 3.8. The dashed straight line is the uncorrected theoretical ratio for SN II ejecta.

Fig. 7.— Comparison of derived SN Ia Fe mass fractions obtained from various observed elemental abundance ratios for inner ($0 - 2'$) and outer ($3 - 12'$) regions. The sulfur-dependent ratios have been corrected by reducing the theoretical sulfur production by a factor of 3.8. The average SN Ia mass fraction derived in this work is denoted μ .

Table 1. Effective Exposure Times

Spectrometer	Exposure Time (kiloseconds)
SIS 0	29.6
SIS 1	23.3
GIS 2	39.8
GIS 3	39.6

Table 2. Spectral Fits^a

Instrument	Region ^b (arcmin)	kT (keV)	Abundance (solar)	χ^2_ν
GIS 1 & 2	0 – 3	$3.54^{+0.11}_{-0.11}$	$0.52^{+0.06}_{-0.06}$	1.04
“	3 – 6	$4.26^{+0.16}_{-0.15}$	$0.39^{+0.06}_{-0.05}$	0.93
“	6 – 9	$4.37^{+0.24}_{-0.23}$	$0.34^{+0.08}_{-0.07}$	1.03
“	9 – 12	$4.31^{+0.38}_{-0.33}$	$0.41^{+0.13}_{-0.12}$	1.07
“	6 – 12	$4.27^{+0.20}_{-0.19}$	$0.35^{+0.07}_{-0.06}$	1.08
“	3 – 12	$4.26^{+0.13}_{-0.12}$	$0.38^{+0.04}_{-0.04}$	0.97
“	0 – 2	$3.39^{+0.14}_{-0.13}$	$0.54^{+0.08}_{-0.08}$	0.96
SIS 1 & 2	0 – 2	$3.14^{+0.09}_{-0.08}$	$0.48^{+0.06}_{-0.05}$	1.11
“	2 – 4	$3.71^{+0.11}_{-0.10}$	$0.40^{+0.05}_{-0.05}$	1.24
“	4 – 6	$4.22^{+0.19}_{-0.17}$	$0.26^{+0.07}_{-0.06}$	1.10
“	6 – 8	$4.35^{+0.25}_{-0.23}$	$0.32^{+0.08}_{-0.09}$	1.04
“	8 – 10	$4.80^{+0.43}_{-0.37}$	$0.42^{+0.15}_{-0.14}$	1.20
“	10 – 12	$4.45^{+0.50}_{-0.43}$	$0.48^{+0.23}_{-0.20}$	0.95
“	2 – 12	$4.09^{+0.09}_{-0.09}$	$0.35^{+0.03}_{-0.03}$	1.36
“	0 – 3	$3.31^{+0.07}_{-0.07}$	$0.45^{+0.04}_{-0.04}$	1.10
“	3 – 6	$4.06^{+0.13}_{-0.13}$	$0.33^{+0.05}_{-0.05}$	1.24
“	6 – 9	$4.51^{+0.24}_{-0.22}$	$0.31^{+0.08}_{-0.07}$	1.16
“	9 – 12	$4.61^{+0.40}_{-0.36}$	$0.48^{+0.16}_{-0.15}$	0.90
“	6 – 12	$4.53^{+0.20}_{-0.19}$	$0.35^{+0.07}_{-0.06}$	1.16
“	2 – 6	$3.89^{+0.09}_{-0.09}$	$0.36^{+0.04}_{-0.04}$	1.33
“	3 – 12	$4.28^{+0.11}_{-0.11}$	$0.35^{+0.04}_{-0.04}$	1.29
ALL ^c	0 – 3	$3.40^{+0.06}_{-0.06}$	$0.49^{+0.03}_{-0.03}$	1.07
“	0 – 3*	$3.70^{+0.01}_{-0.08}$	$0.51^{+0.04}_{-0.03}$	1.06
“	3 – 6	$4.17^{+0.10}_{-0.09}$	$0.37^{+0.04}_{-0.04}$	1.04
“	6 – 9	$4.46^{+0.16}_{-0.16}$	$0.32^{+0.05}_{-0.05}$	1.07
“	9 – 12	$4.44^{+0.26}_{-0.24}$	$0.42^{+0.09}_{-0.09}$	1.02
“	6 – 12	$4.40^{+0.13}_{-0.13}$	$0.34^{+0.05}_{-0.04}$	1.11
“	3 – 12	$4.28^{+0.08}_{-0.08}$	$0.36^{+0.03}_{-0.03}$	1.07
“	0 – 2	$3.24^{+0.07}_{-0.06}$	$0.53^{+0.04}_{-0.04}$	1.03
“	0 – 2*	$3.37^{+0.08}_{-0.09}$	$0.54^{+0.05}_{-0.05}$	1.03

^aErrors are 90% confidence limits

^bDistance from the X-ray center

^cSimultaneous fittings of SIS 0 & 1, GIS 2 & 3

*same as above but with an extra cooling flow component

Table 3. Individual Elemental Abundances^a

Element	Region			gradient?
	0 – 2'	0 – 3'	3 – 12'	
O	$0.47^{+0.39}_{-0.37}$	$0.61^{+0.33}_{-0.32}$	$0.49^{+0.47}_{-0.29}$	
Ne	$0.88^{+0.45}_{-0.40}$	$0.91^{+0.36}_{-0.33}$	$0.63^{+0.48}_{-0.28}$	
Mg	$0.20^{+0.34}_{-0.20}$	$0.33^{+0.27}_{-0.29}$	$0.01^{+0.35}_{-0.01}$	
Si	$0.83^{+0.18}_{-0.17}$	$0.83^{+0.12}_{-0.14}$	$0.67^{+0.19}_{-0.13}$	
S	$0.59^{+0.19}_{-0.20}$	$0.49^{+0.16}_{-0.16}$	$0.19^{+0.15}_{-0.17}$	✓
Ar	≤ 0.3	≤ 0.3	$0.01^{+0.45}_{-0.01}$	
Ca	$0.33^{+0.48}_{-0.33}$	$0.22^{+0.61}_{-0.22}$	$0.31^{+0.49}_{-0.31}$	
Fe	$0.53^{+0.05}_{-0.05}$	$0.50^{+0.04}_{-0.04}$	$0.36^{+0.03}_{-0.03}$	✓
Ni	$2.51^{+0.67}_{-0.80}$	$1.94^{+0.58}_{-0.64}$	$0.96^{+0.79}_{-0.60}$	✓

^aErrors are 90% confidence limits

Table 4. Elemental Abundance Ratios^a

Element Ratio	grad	Region			Theory ^b		Fe Mass Fraction from SN Ia		
		0 – 2'	0 – 3'	3 – 12'	SN Ia	SN II	0 – 2'	0 – 3'	3 – 12'
O/Fe		$0.91^{+0.44}_{-0.44}$	$1.23^{+0.39}_{-0.39}$	$1.58^{+0.62}_{-0.60}$	0.037	3.82	$0.84^{+0.13}_{-0.13}$	$0.74^{+0.12}_{-0.12}$	$0.64^{+0.18}_{-0.18}$
Ne/Fe		$1.64^{+0.53}_{-0.45}$	$1.77^{+0.66}_{-0.38}$	$2.00^{+0.66}_{-0.38}$	0.006	2.69	$0.38^{+0.17}_{-0.20}$	$0.33^{+0.14}_{-0.24}$	$0.25^{+0.30}_{-0.23}$
Si/Fe		$1.58^{+0.22}_{-0.22}$	$1.68^{+0.21}_{-0.17}$	$1.92^{+0.29}_{-0.27}$	0.538	3.53	$0.65^{+0.07}_{-0.08}$	$0.61^{+0.06}_{-0.07}$	$0.53^{+0.09}_{-0.09}$
Ni/Fe		$4.86^{+1.02}_{-0.96}$	$4.01^{+0.84}_{-0.78}$	$2.88^{+1.12}_{-1.05}$	4.758	1.65	$1.00^{+0.00}_{-0.27}$	$0.76^{+0.24}_{-0.25}$	$0.39^{+0.35}_{-0.34}$
O/Si		$0.58^{+0.72}_{-0.29}$	$0.73^{+0.58}_{-0.24}$	$0.82^{+1.47}_{-0.33}$	0.068	1.1	$0.86^{+0.10}_{-0.86}$	$0.77^{+0.13}_{-0.77}$	$0.68^{+0.22}_{-0.68}$
Si/Ni	✓	$0.33^{+0.08}_{-0.08}$	$0.42^{+0.1}_{-0.09}$	$0.67^{+0.27}_{-0.26}$	0.113	2.14	$0.74^{+0.07}_{-0.09}$	$0.65^{+0.08}_{-0.09}$	$0.47^{+0.14}_{-0.20}$
Ne/Si ^c		$1.04^{+0.36}_{-0.31}$	$1.05^{+0.41}_{-0.24}$	$1.05^{+0.35}_{-0.31}$	0.012	0.76			
S/Fe	✓	$1.10^{+0.19}_{-0.25}$	$0.98^{+0.22}_{-0.28}$	$0.54^{+0.30}_{-0.29}$	0.585	2.29			
O/S		$0.82^{+0.42}_{-0.43}$	$1.26^{+0.49}_{-0.53}$	$2.92^{+1.98}_{-1.85}$	0.063	1.67			
Ne/S ^c		$1.48^{+0.53}_{-0.52}$	$1.81^{+0.79}_{-0.64}$	$3.72^{+2.35}_{-2.16}$	0.001	1.18			
Si/S ^c	✓	$1.43^{+0.30}_{-0.37}$	$1.72^{+0.43}_{-0.52}$	$3.55^{+2.03}_{-1.88}$	0.919	1.54			
S/Ni		$0.23^{+0.06}_{-0.07}$	$0.24^{+0.07}_{-0.08}$	$0.19^{+0.13}_{-0.12}$	0.123	1.39			

^aErrors are propagated 1σ errors

^bSN Ia: Nomoto et al (1997a); SN II: Nomoto et al (1997b)

^cSignificantly out of theoretical boundaries

Table 5. Gas & Iron Masses (in M_{\odot}) from SN Ia & II

		Region	
	0 – 2'	0 – 3'	3 – 12'
M_{gas}	2.2×10^{12}	5.1×10^{12}	4.5×10^{13}
M_{Fe}	2.4×10^9	5.1×10^9	3.2×10^{10}
$M_{\text{FeSN Ia}}$	$(1.7 \pm 0.3) \times 10^9$	$(3.2 \pm 0.6) \times 10^9$	$(1.5 \pm 0.6) \times 10^{10}$
$M_{\text{FeSN II}}$	$(0.6 \pm 0.3) \times 10^9$	$(1.9 \pm 0.3) \times 10^9$	$(1.7 \pm 0.3) \times 10^{10}$
$M_{\text{FeSN Ia}}/M_{\text{Fe}}$	0.72 ± 0.11	0.65 ± 0.12	0.46 ± 0.17
$A_{\text{FeSN Ia}}$ (solar)	0.38 ± 0.07	0.33 ± 0.07	0.17 ± 0.06
$A_{\text{FeSN II}}$ (solar)	0.15 ± 0.06	0.18 ± 0.06	0.19 ± 0.06
$M_{\text{FeSN Ia}}/L_{B_{\text{E+S0}}}$	0.015 ± 0.01	0.018 ± 0.01	0.023 ± 0.018
$M_{\text{FeSN II}}/L_{(B_{\text{E+S0}})}$	0.005 ± 0.003	0.010 ± 0.005	0.028 ± 0.018
$\text{SNR}_{\text{Ia}}(\text{SNU})$	2.0 ± 1.3	2.4 ± 1.3	3.1 ± 2.4
$\text{SNR}_{\text{II}}(\text{SNU})$	5.5 ± 3.3	11 ± 6	31 ± 20

Figure 1a - GIS Spectra for Inner and Outer Regions

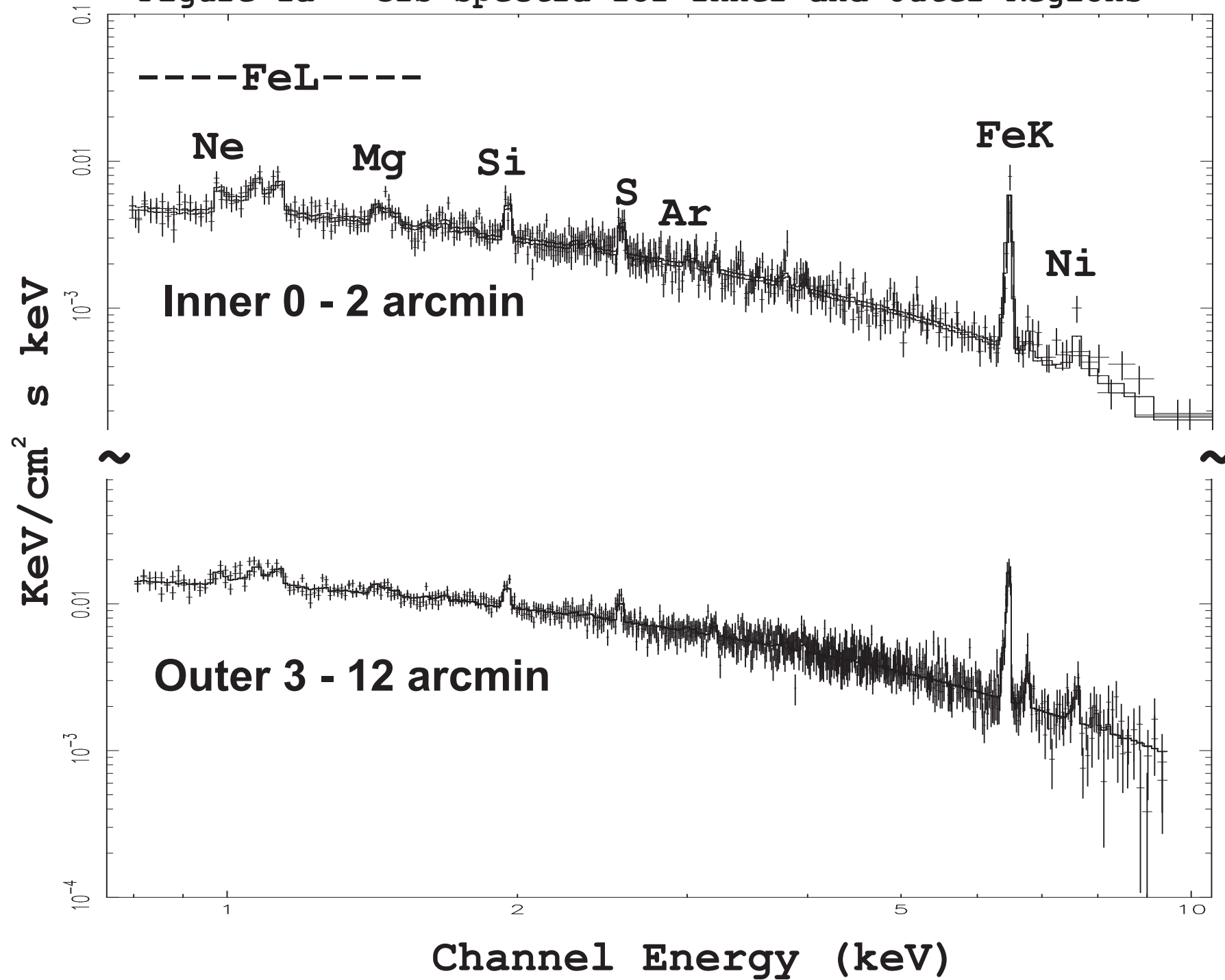
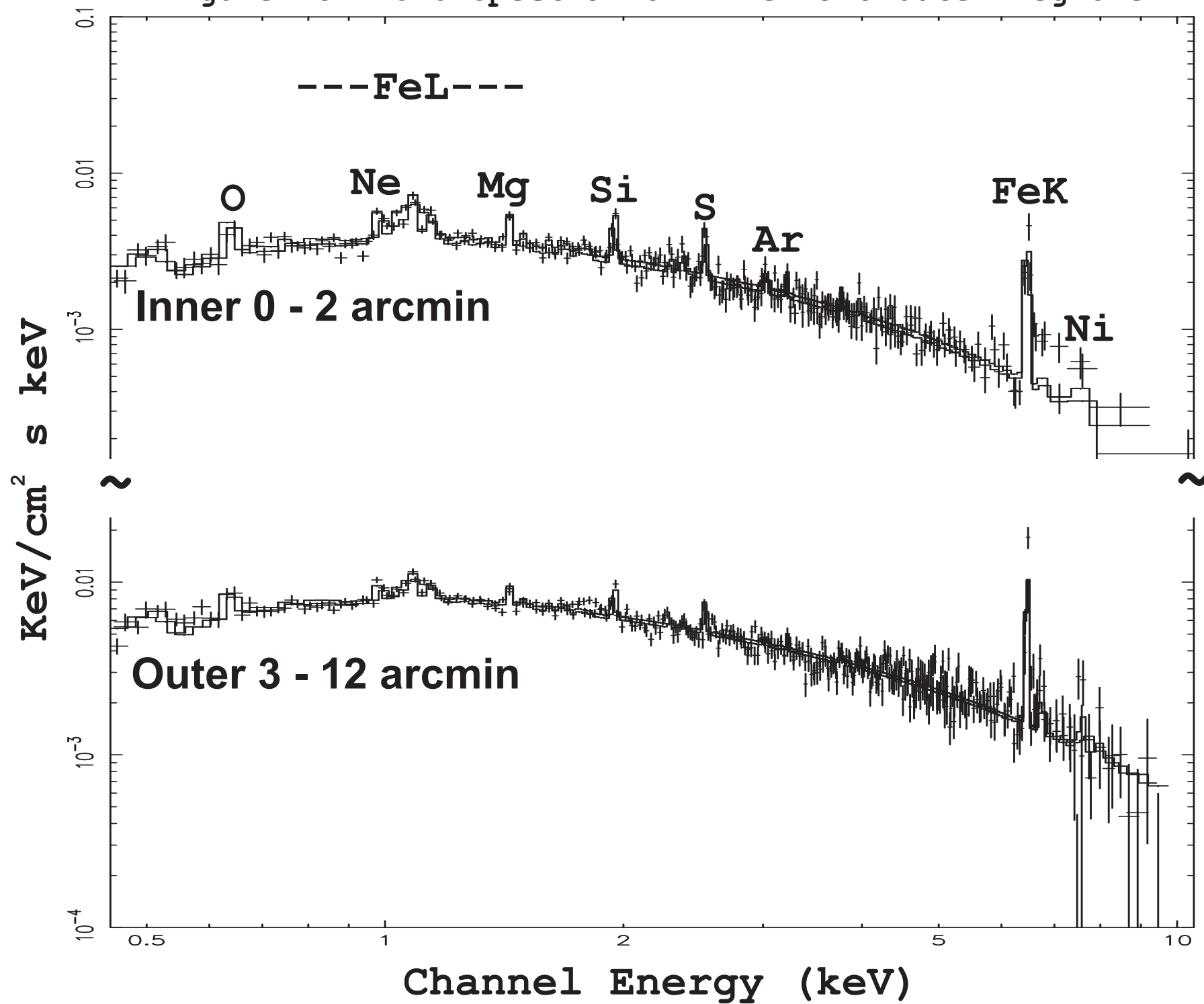
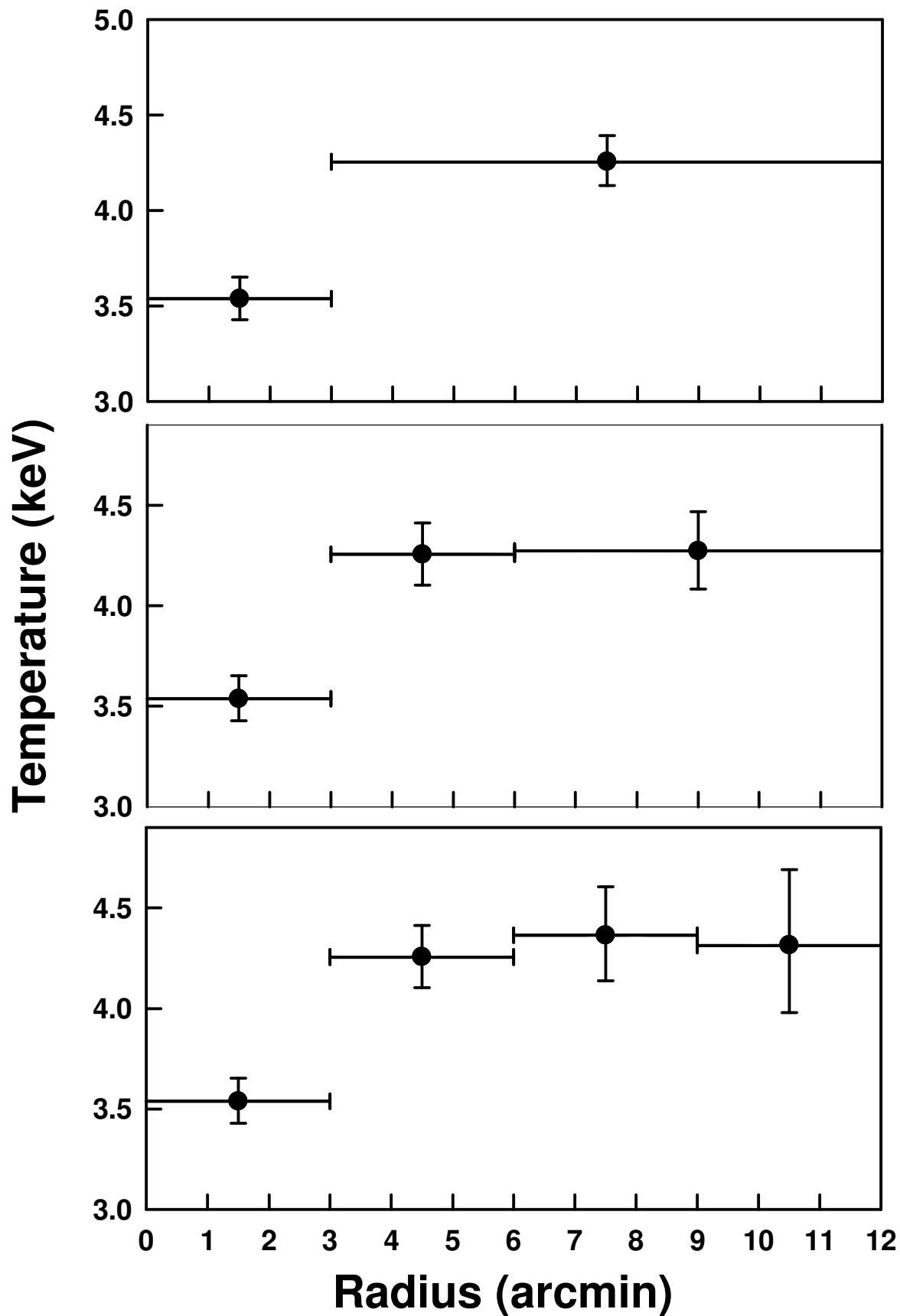


Figure 1b - SIS Spectra for Inner and Outer Regions



**Figure 2.a - Temperature Distribution
GIS 2&3 - Simultaneous Fitting**



**Figure 2.b - Abundance distribution
GIS 2&3 - Simultaneous Fitting**

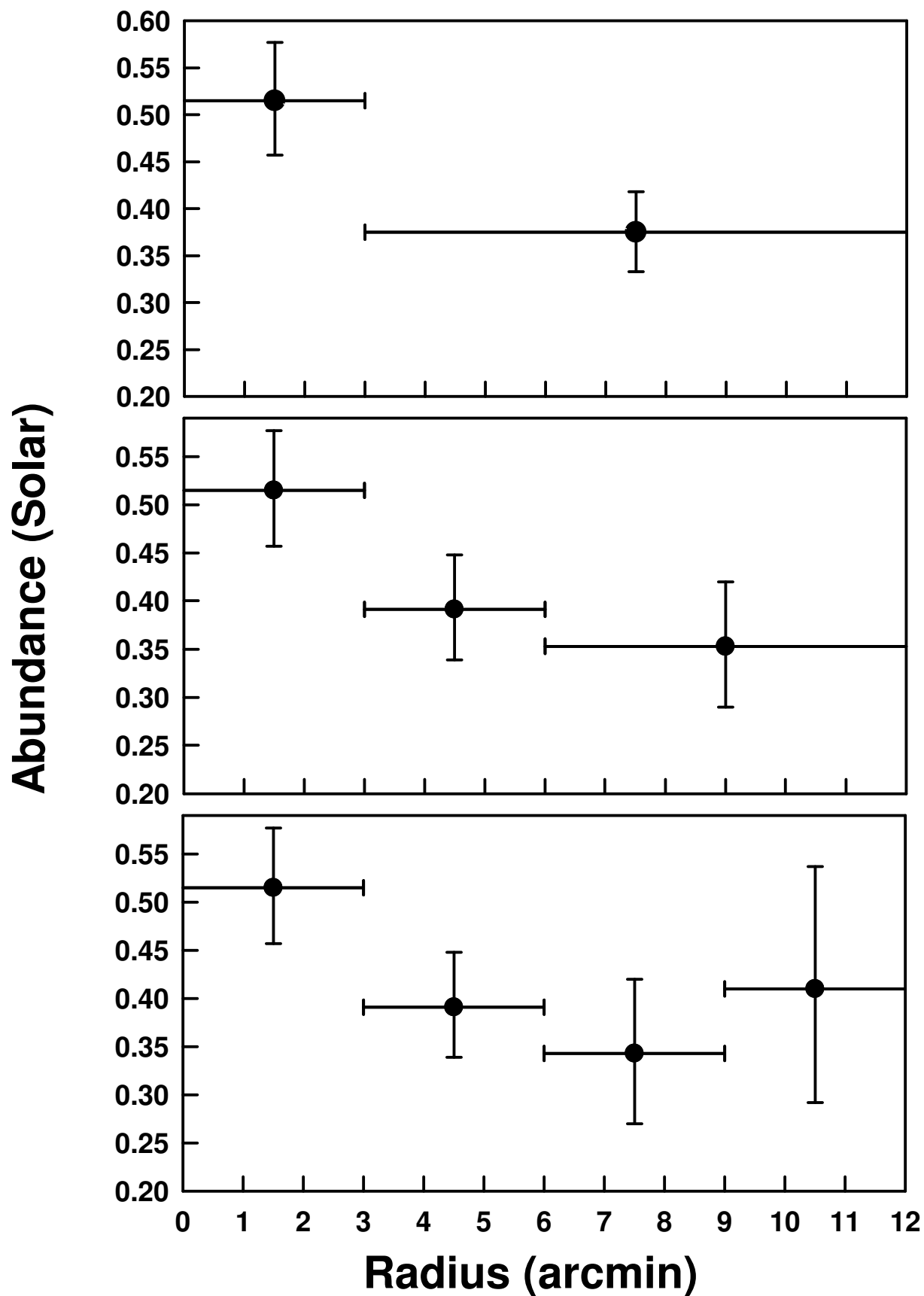


**Figure 3.a - Temperature Distribution
SIS 0&1 - Simultaneous Fitting**

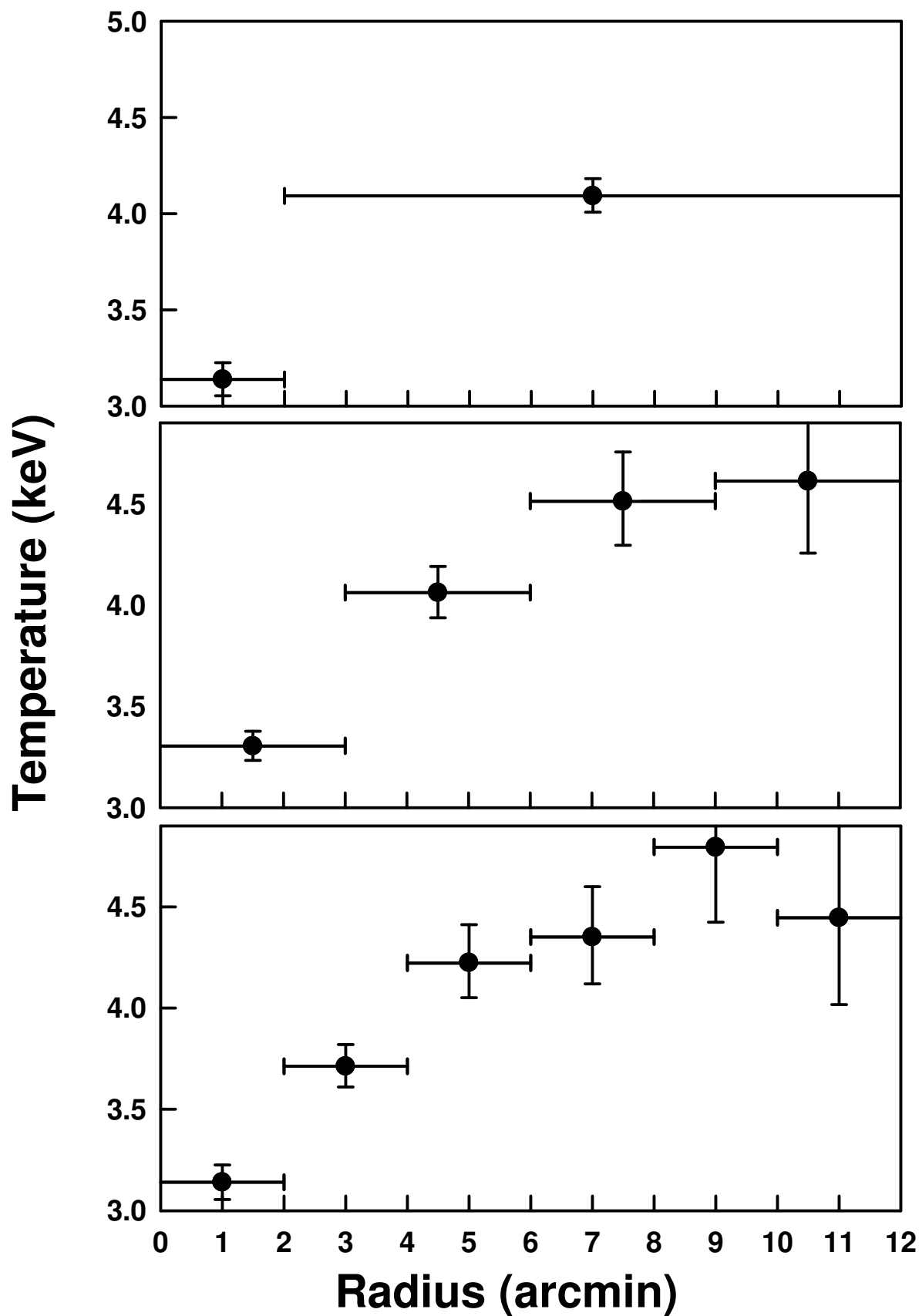


**Figure 3.b - Abundance Distribution
SIS 0&1 - Simultaneous Fitting**

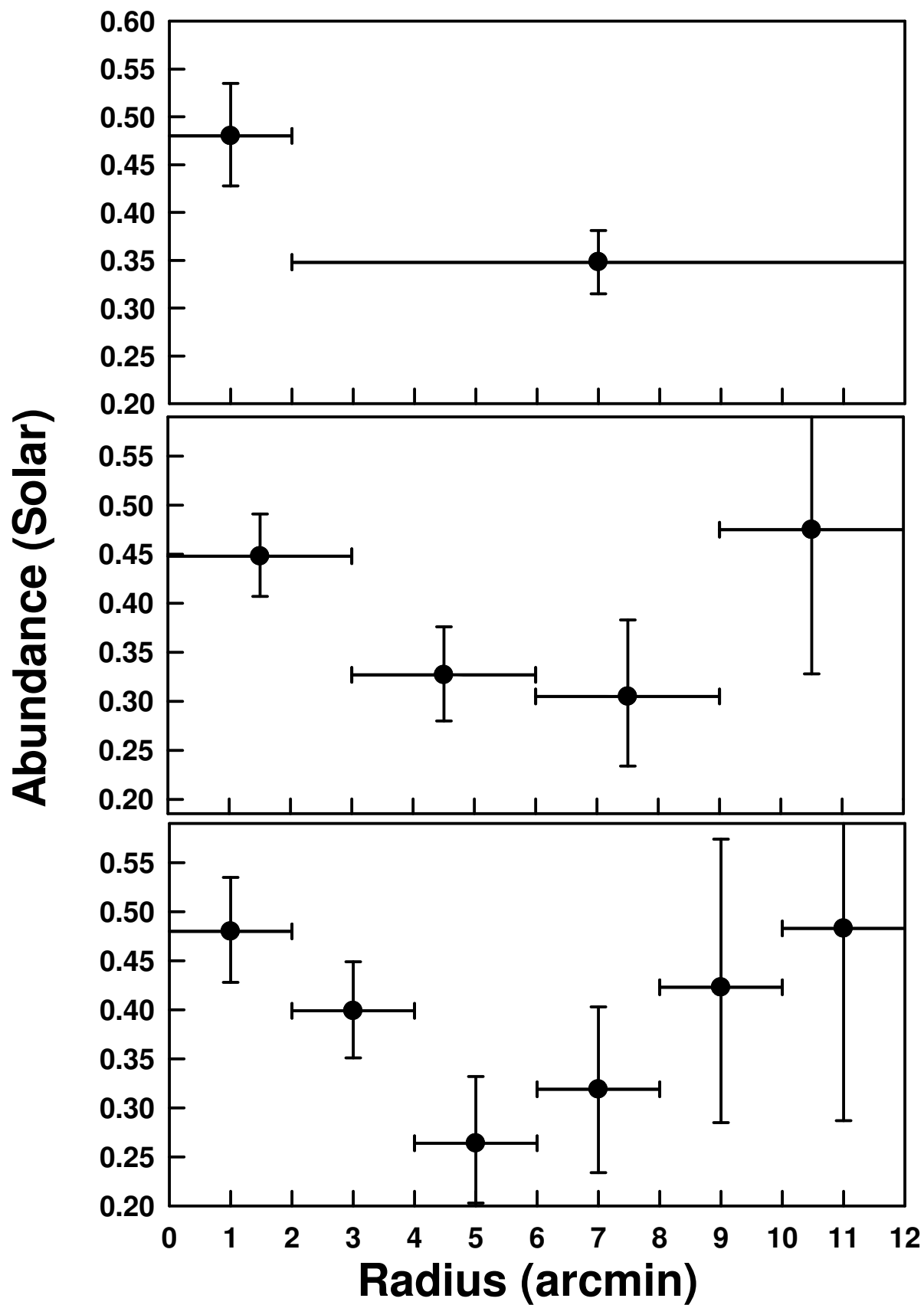


**Figure 4.a - Temperature Distribution
SIS 0 & 1 and GIS 2 & 3
Simultaneous Fitting**

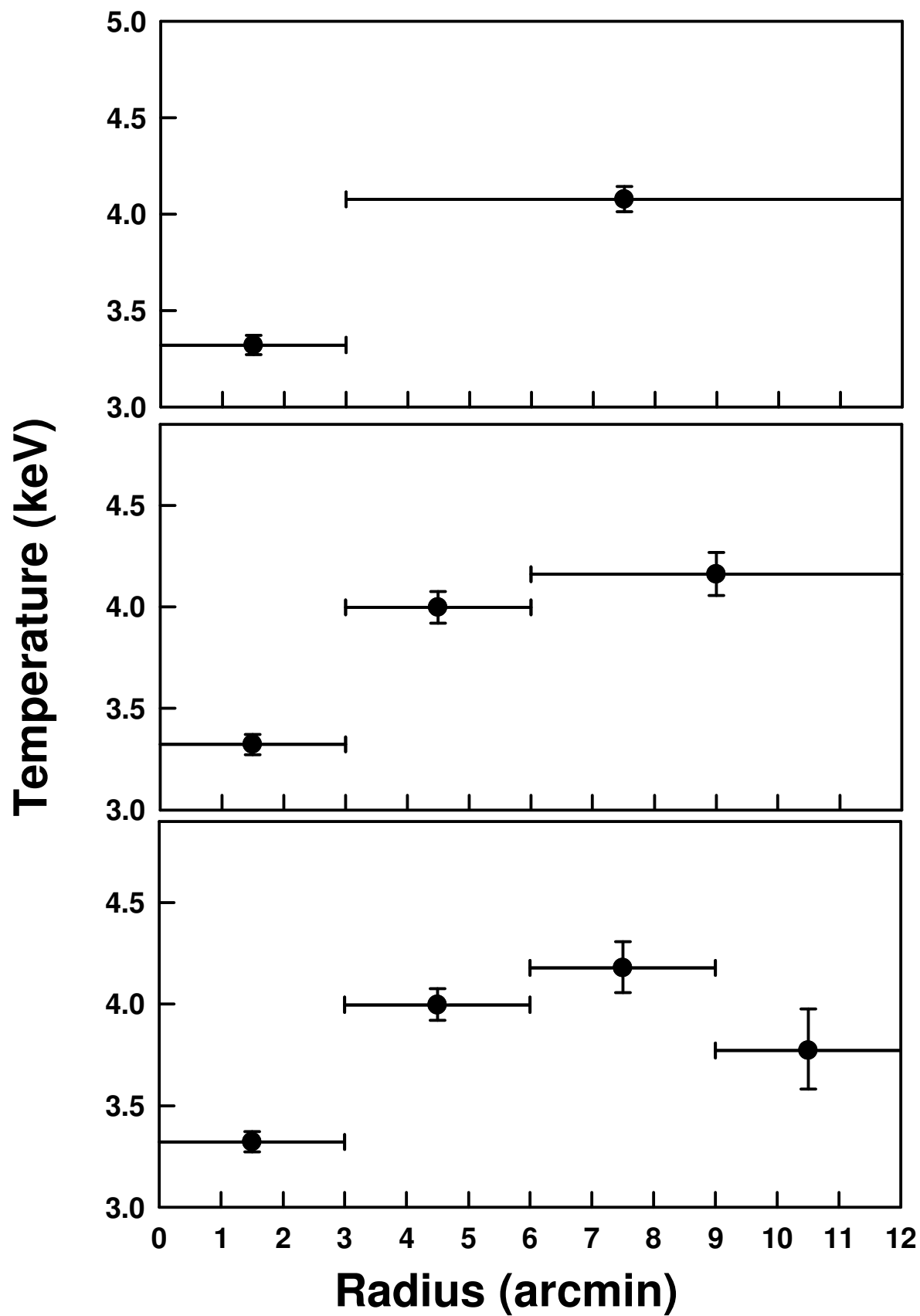


**Figure 4.b - Abundance Distribution
SIS 0 & 1 and GIS 2 & 3
Simultaneous Fitting**

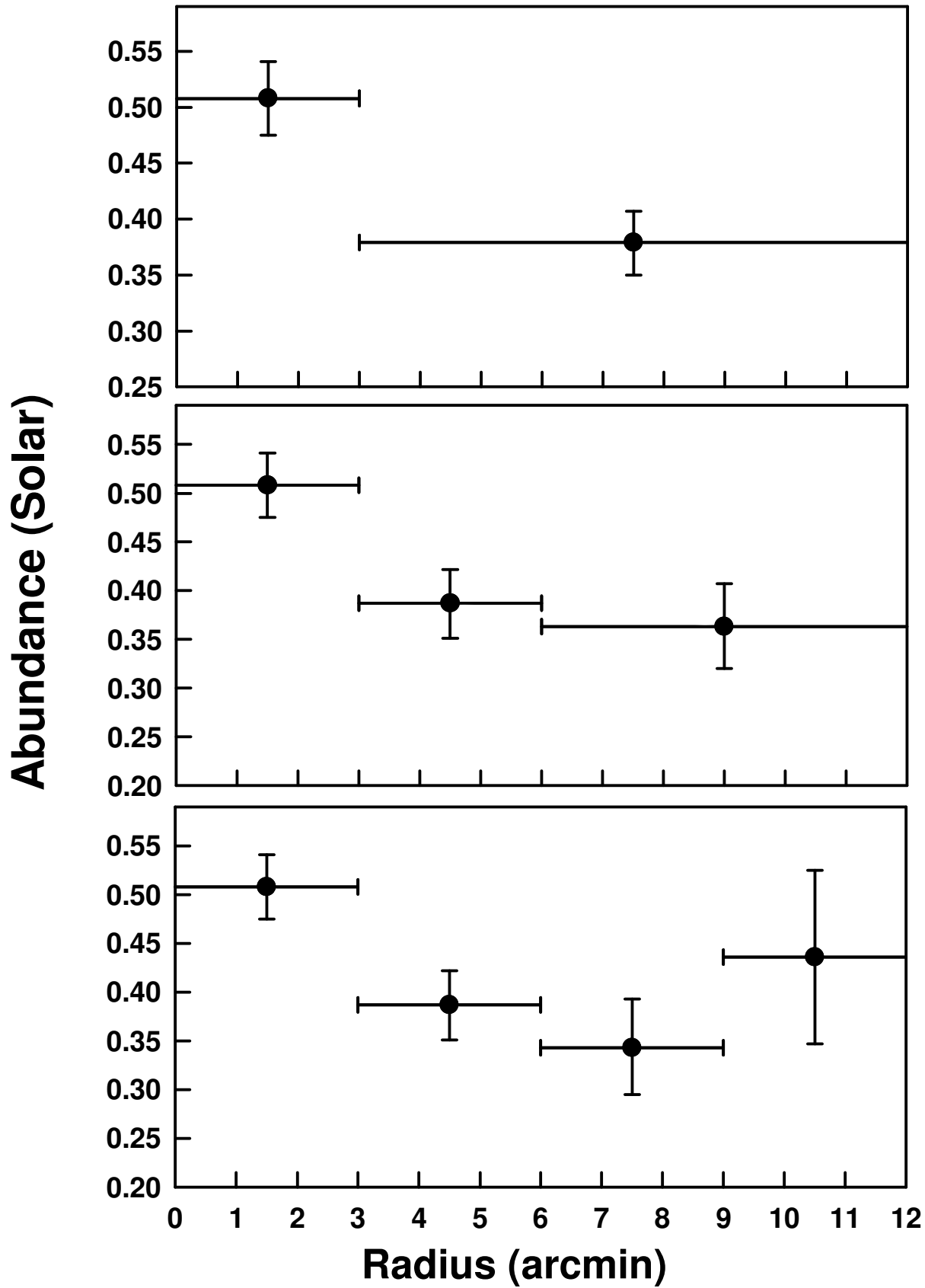


Figure 5 – Confidence contours for the Two Innermost Regions

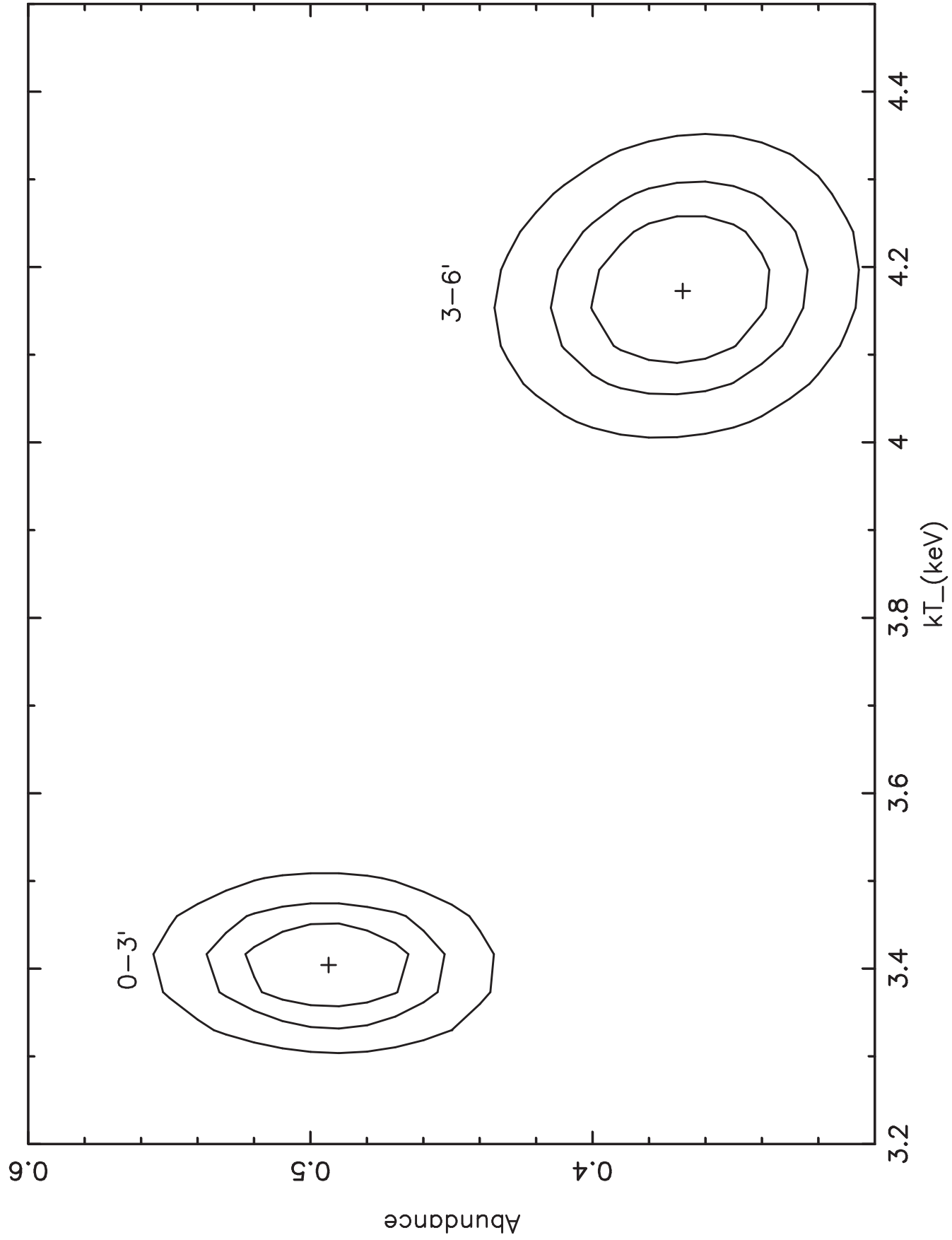


Figure 6 – Confidence contours for Si & S

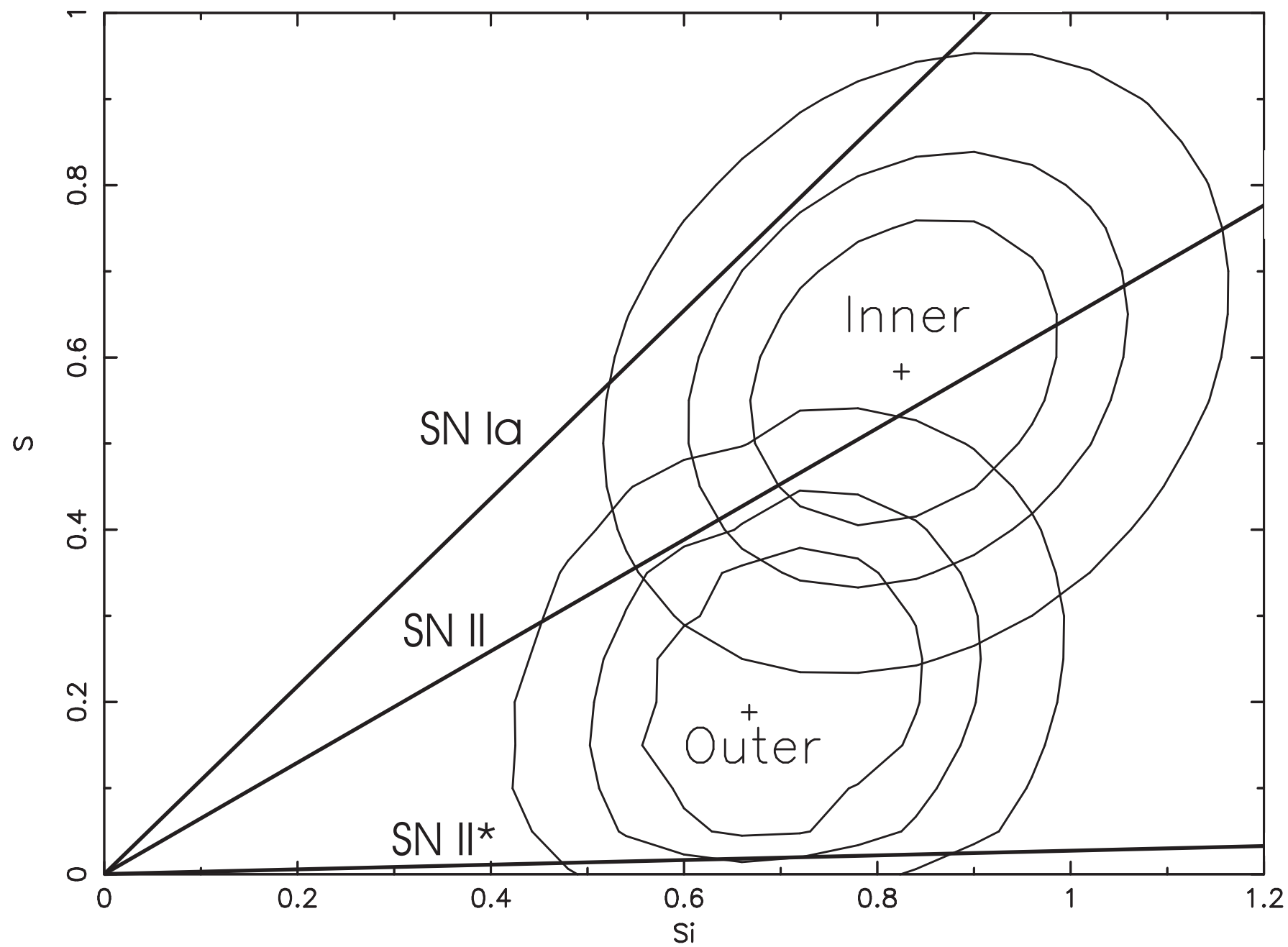


Figure 7 - SN Ia Fe Mass Fractions

